HQ-VAE: Hierarchical Discrete Representation Learning with Variational Bayes

Anonymous authors
Paper under double-blind review

Abstract

Vector quantization (VQ) is a technique to deterministically learn features with discrete codebook representations. It is commonly achieved with a variational autoencoding model, VQ-VAE, which is further extended to hierarchical structures for high-fidelity reconstruction. However, training hierarchical extensions of VQ-VAE is often unstable, where the codebook is not efficiently used to express data well, hence deteriorates reconstruction accuracy. To mitigate this problem, we propose a novel framework to stochastically learn hierarchical discrete representation on the basis of the variational Bayes framework, called hierarchically quantized variational autoencoder (HQ-VAE). HQ-VAE naturally unifies the hierarchical variants of VQ-VAE such as VQ-VAE-2 and residual-quantized VAE (RQ-VAE) and stabilizes their training in a Bayesian scheme. Our comprehensive experiments on image datasets show that HQ-VAE enhances codebook usage and improves reconstruction performance. We also validate HQ-VAE in terms of its applicability even to a different modality with an audio dataset.

1 Introduction

Learning representations with discrete features is one of the core technologies in the field of deep learning. Vector quantization (VQ) for approximating continuous features with a set of finite trainable code vectors is a common technique to achieve such representation Toderici et al. (2016); Theis et al. (2017); Agustsson et al. (2017). It has been widely adopted in several active applications including neural codecs, e.g., image compression Williams et al. (2020); Wang et al. (2022) and audio codec Zeghidour et al. (2021); Défossez et al. (2022). VQ-based representation methods have been improved with successful deep generative modeling, especially denoising diffusion probabilistic models Sohl-Dickstein et al. (2015); Ho et al. (2020); Song et al. (2020); Dhariwal & Nichol (2021); Hoogeboom et al. (2021); Austin et al. (2021) and autoregressive models van den Oord et al. (2016); Chen et al. (2018); Child et al. (2019). Learning discrete features of target data among finitely many representations can ignore redundant information, and such a lossy compression can assist with training deep generative models on large-scale data. After compression, one can train another deep generative model, which is called a prior model, on the compressed representation instead of the raw data. This approach has achieved attractive results in various tasks, e.g., unconditional generation tasks Razavi et al. (2019); Dhariwal et al. (2020); Esser et al. (2021b;a); Rombach et al. (2022), text-to-image generation Ramesh et al. (2021); Gu et al. (2022); Lee et al. (2022a) and textually guided audio generation Yang et al. (2022); Kreuk et al. (2022). Note that the compression performance of VQ limits the overall generation performance regardless of the performance of the prior model.

VQ is usually achieved with the model vector quantized variational autoencoder (VQ-VAE) van den Oord et al. (2017). In VQ-VAE, an input is first encoded and quantized with the code vectors, which extracts the discrete representation of the encoded feature. The discrete representation is then decoded to the data space to recover the original input. Subsequently, advanced studies incorporated the hierarchical structure into the discrete latent space to effectively achieve high-fidelity reconstruction. Razavi et al. (2019) initially extended VQ-VAE to a hierarchical model, which is called VQ-VAE-2. In this model, multi-resolution discrete latent representations are introduced to extract local and global information of the target data. As another type of hierarchical discrete representation, residual quantization (RQ), was proposed to reduce the gap between the feature maps before and after the quantization process Zeghidour et al. (2021); Lee et al. (2022a).

Despite its successes in many tasks, training variants of VQ-VAE is still challenging. It is known that VQ-VAE suffers from codebook collapse, where only few code vectors are used for the representation Kaiser et al. (2018); Roy et al. (2018); Takida et al. (2022b). This inefficiency may deteriorate reconstruction accuracy, hence, limit its applications to downstream tasks. The extension with hierarchical latent representations suffers from the same issue. For example, Dhariwal et al. (2020) reported that it is generally difficult to push information to higher levels in VQ-VAE-2, i.e., codebook collapse often occurs there. Therefore, certain heuristic techniques such as the exponential moving average (EMA) update Polyak & Juditsky (1992) and codebook reset Dhariwal et al. (2020) are usually implemented to mitigate these problems. Takida et al. (2022b) claimed that the issue is triggered because the training scheme of VQ-VAE does not follow the variational Bayes framework but relies on carefully designed heuristics. They proposed stochastically quantized VAE (SQ-VAE), with which the components of VQ-VAE, i.e., the encoder, decoder and code vectors, are trained in the variational Bayes framework with an SQ operator. The model was shown to improve reconstruction performance by preventing the collapse issue thanks to the *self-annealing* effect Takida et al. (2022b), where the SQ process gradually tends to the deterministic one during training. We expect this has the potential to stabilize the training by mitigating this problem even in the hierarchical model, which may lead to improving reconstruction performance with more efficient codebook usage.

We propose *Hierarchically Quantized VAE* (*HQ-VAE*), a general variational Bayesian model for learning hierarchical discrete latent representations. Figure 1 illustrates the overall architecture of HQ-VAE. The novel hierarchical structure in HQ-VAE consists of *bottom-up* and *top-down* path pair, which assists with capturing local and global information of data. We instantiate the generic HQ-VAE by introducing two types of *top-down* layers. These two layers formulate the hierarchical structures of VQ-VAE-2 and residual-quantized VAE (RQ-VAE) within the variational scheme, which we call *SQ-VAE-2* and *RSQ-VAE*, respectively. HQ-VAE can be viewed as an extension of SQ-VAE with hierarchy, hence, shares similar favorable properties of SQ-VAE (e.g., the *self-annealing* effect). In this sense, HQ-VAE unifies the current well-known VQ models in the variational Bayes framework, which provides a novel training mechanism. We empirically show HQ-VAE improves upon conventional methods in the vision and audio domains.

Throughout this paper, the uppercase letters (P, Q) and the lowercase letters (p, q) denote the probability mass functions and probability density functions, respectively; calligraphy letters ($\mathcal{P}$, $\mathcal{Q}$) denote the joint probabilistic distributions of both continuous and discrete random variables; bold lowercase and uppercase letters (e.g., $\boldsymbol{x}$ and $\boldsymbol{Y}$) respectively denote vectors and matrices, and the ith column vector in $\boldsymbol{Y}$ is written as $\boldsymbol{y}_i$; $[N]$ denotes a set of positive integers no more than $N \in \mathbb{N}$. Finally, we use $\mathcal{J}$ and $\mathcal{L}$ for the objective functions of HQ-VAE and conventional ones, respectively.

2 Background

We first revisit VQ-VAE and its extensions to hierarchical latent models. We then review SQ-VAE which serves as the foundation framework of HQ-VAE.

2.1 VQ-VAE

To discretely represent observations $\boldsymbol{x} \in \mathbb{R}^D$, a codebook $\boldsymbol{B}$ is introduced, which consists of finite trainable code vectors $\{\boldsymbol{b}_k\}_{k=1}^K$ ($\boldsymbol{b}_k \in \mathbb{R}^{d_b}$). A discrete latent variable $\boldsymbol{Z}$ is constructed to be in the d_z-tuple of $\boldsymbol{B}$, i.e., $\boldsymbol{Z} \in \boldsymbol{B}^{d_z}$, which is later decoded to generate data samples. To connect the observation and latent representaion, a deterministic encoder and decoder pair is introduced, where the encoder maps $\boldsymbol{x}$ to $\boldsymbol{Z}$ and the decoder recovers $\boldsymbol{x}$ from $\boldsymbol{Z}$ by a decoding function $\boldsymbol{f}_{\boldsymbol{\theta}} : \mathbb{R}^{d_b \times d_z} \to \mathbb{R}^D$. For the encoder, an encoding function, denoted as $\boldsymbol{G}_{\boldsymbol{\phi}} : \mathbb{R}^D \to \mathbb{R}^{d_b \times d_z}$, and a deterministic quantization operator are introduced. The encoding function first maps $\boldsymbol{x}$ to $\hat{\boldsymbol{Z}} \in \mathbb{R}^{d_b \times d_z}$, then the quantization operator finds the nearest neighbor of $\hat{\boldsymbol{z}}_i$ for $i \in [d_z]$, i.e., $\boldsymbol{z}_i = \arg\min_{\boldsymbol{b}_k} \|\hat{\boldsymbol{z}}_i - \boldsymbol{b}_k\|_2^2$. The trainable components (the encoder, decoder, and codebook) are learned by minimizing the objective

$$\mathcal{L}_{\text{VQ-VAE}} = \|\boldsymbol{x} - \boldsymbol{f}_{\boldsymbol{\theta}}(\boldsymbol{Z})\|_2^2 + \beta \|\hat{\boldsymbol{Z}} - \text{sg}[\boldsymbol{Z}]\|_F^2, \tag{1}$$

where $\text{sg}[\cdot]$ is the stop-gradient operator and β is a hyperparameter balancing the two terms. The codebook is updated by applying the EMA update to $\|\text{sg}[\hat{\boldsymbol{Z}}] - \boldsymbol{Z}\|_F^2$.

VQ-VAE-2. To model both local and global information separately, VQ-VAE-2 adopts a hierarchical structure for vector quantization Razavi et al. (2019). The model consists of multiple levels of latents so that top levels have global information while bottom levels are focused on local information, conditioned on the top levels. The training of the model follows the same scheme as the original VQ-VAE (e.g., stop-gradient, the EMA update, and deterministic quantization).

RQ-VAE. RQ provides a finer approximation of $\boldsymbol{Z}$ by taking into account the information of quantization gaps (residuals) Zeghidour et al. (2021); Lee et al. (2022a). With RQ, L code vectors are assigned to each vector $\boldsymbol{z}_i$ ($i \in [d_z]$), instead of increasing the codebook size K. To achieve multiple assignments, RQ repeatedly quantizes the target feature and computes quantization residuals, denoted as $\boldsymbol{R}_l$. Namely, the following procedure is repeated L times starting with $\boldsymbol{R}_0 = \hat{\boldsymbol{Z}}$: $\boldsymbol{z}_{l,i} = \arg\min_{\boldsymbol{b}_k} \|\boldsymbol{r}_{l-1,i} - \boldsymbol{b}_k\|_2^2$ and $\boldsymbol{R}_l = \boldsymbol{R}_{l-1} - \boldsymbol{Z}_l$. By repeating RQ, the discrete representation is expected to be refined in a coarse-to-fine manner. Finally, RQ discretely approximates the encoded variable as $\hat{\boldsymbol{Z}} \approx \sum_{l=1}^{L} \boldsymbol{Z}_l$, where the conventional VQ is regarded as a special case of RQ with $L = 1$.

2.2 SQ-VAE

SQ-VAE Takida et al. (2022b) also has deterministic encoding/decoding functions and a trainable codebook. However, unlike the deterministic quantization scheme of VQ and RQ, SQ-VAE designs an SQ procedure for the encoded features following the variational Bayes framework. More precisely, it defines a stochastic dequantization process $p_{s^2}(\tilde{\boldsymbol{z}}_i|\boldsymbol{Z}) = \mathcal{N}(\tilde{\boldsymbol{z}}_i; \boldsymbol{z}_i, s^2\boldsymbol{I})$, which converts a discrete variable $\boldsymbol{z}_i$ into a continuous one $\tilde{\boldsymbol{z}}_i$ by adding Gaussian noise with a learnable variance s^2. By Bayes' rule, it associates with a reverse operation, i.e., SQ, which is given by $\hat{P}_{s^2}(\boldsymbol{z}_i = \boldsymbol{b}_k|\tilde{\boldsymbol{Z}}) \propto \exp\left(-\frac{\|\tilde{\boldsymbol{z}}_i - \boldsymbol{b}_k\|_2^2}{2s^2}\right)$. Thanks to this variational framework, the degree of the stochasticity in the quantization scheme becomes adaptive. This allows SQ-VAE to benefit from the effect of *self-annealing*, where the SQ process gradually approaches the deterministic one as s^2 decreases. This generally improves the efficiency of codebook usage.

3 Hierarchically quantized VAE

In this section, we formulate the generic HQ-VAE model, which learns hierarchical discrete latent representation in the variational Bayes framework. It serves as a backbone of the instantiations of HQ-VAE presented in Section 4.

To achieve hierarchical discrete representation of depth L, we first introduce L groups of discrete latent variables, which are denoted as $\boldsymbol{Z}_{1:L} := \{\boldsymbol{Z}_l\}_{l=1}^{L}$. For each $l \in [L]$ we introduce a trainable codebook $\boldsymbol{B}_l := \{\boldsymbol{b}_k^l\}_{k=1}^{K_l}$, consisting of K_l d_b-dimensional code vectors, i.e., $\boldsymbol{b}_k^l \in \mathbb{R}^{d_b}$ for $k \in [K_l]$. The variable $\boldsymbol{Z}_l$ is represented as a d_l-tuple of the code vectors in $\boldsymbol{B}_l$; namely, $\boldsymbol{Z}_l \in \boldsymbol{B}_l^{d_l}$. Similarly to conventional VAEs, the latent variable of each group is assumed to follow a pre-defined prior mass function. We set the prior as an i.i.d. uniform distribution, defined as $P(\boldsymbol{z}_{l,i} = \boldsymbol{b}_k) = 1/K_l$ for $i \in [d_l]$. The probabilistic decoder is set as a normal distribution with a trainable isotropic covariance matrix as $p_{\boldsymbol{\theta}}(\boldsymbol{x}|\boldsymbol{Z}_{1:L}) = \mathcal{N}(\boldsymbol{x}; \boldsymbol{f}_{\boldsymbol{\theta}}(\boldsymbol{Z}_{1:L}), \sigma^2\boldsymbol{I})$ with a decoding function $\boldsymbol{f}_{\boldsymbol{\theta}} : \mathbb{R}^{d_b \times d_1} \oplus \cdots \oplus \mathbb{R}^{d_b \times d_L} \to \mathbb{R}^D$. It decodes latent variables sampled from the prior to generate instances. Here, the exact evaluation of $P_{\boldsymbol{\theta}}(\boldsymbol{Z}_{1:L}|\boldsymbol{x})$ is required to train the generative model with the maximum likelihood. However, it is intractable in practice. Thus, we introduce an approximated posterior on $\boldsymbol{Z}_{1:L}$ given $\boldsymbol{x}$ and derive the evidence lower bound (ELBO) for maximization instead.

Inspired by hierarchical Gaussian VAEs Sønderby et al. (2016); Vahdat & Kautz (2020); Child (2021), HQ-VAE consists of *bottom-up* and *top-down* paths, as shown in Figure 1a. The approximated posterior has the *top-down* structure ($\boldsymbol{Z}_1 \to \boldsymbol{Z}_2 \to \cdots \to \boldsymbol{Z}_L$). For this process, the *bottom-up* path first generates features

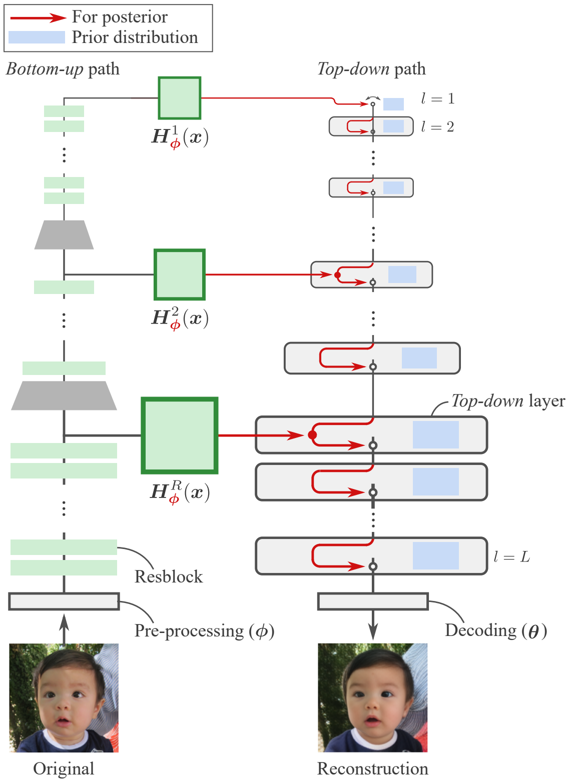
For posterior
Prior distribution
Bottom-up path
Top-down path
$l=1$
$l=2$
$\boldsymbol{H}^1_{\boldsymbol{\phi}}(\boldsymbol{x})$
$\boldsymbol{H}^2_{\boldsymbol{\phi}}(\boldsymbol{x})$
Top-down layer
$\boldsymbol{H}^R_{\boldsymbol{\phi}}(\boldsymbol{x})$
$l=L$
Resblock
Pre-processing (ϕ)
Decoding ($\boldsymbol{\theta}$)
Original
Reconstruction

(a) Overview of HQ-VAE.

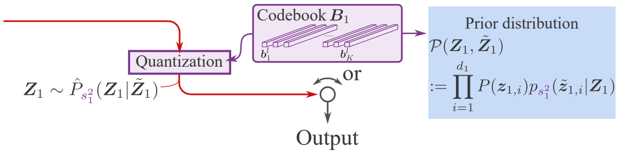
Codebook $\boldsymbol{B}_1$
b_1^1
b_K^1
Quantization
$\boldsymbol{Z}_1 \sim \hat{P}_{s_1^2}(\boldsymbol{Z}_1|\tilde{\boldsymbol{Z}}_1)$
or
Output
Prior distribution
$\mathcal{P}(\boldsymbol{Z}_1, \tilde{\boldsymbol{Z}}_1)$
$:= \prod_{i=1}^{d_1} P(\boldsymbol{z}_{1,i}) p_{s_1^2}(\tilde{\boldsymbol{z}}_{1,i}|\boldsymbol{Z}_1)$

(b) First *top-down* layer.

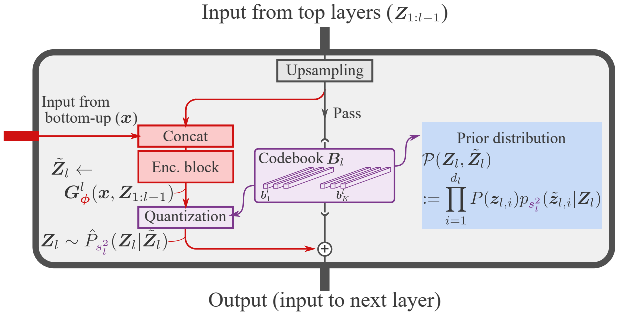
Input from top layers ($\boldsymbol{Z}_{1:l-1}$)
Upsampling
Input from bottom-up ($\boldsymbol{x}$)
Pass
Concat
Enc. block
$\tilde{\boldsymbol{Z}}_l \leftarrow$
$\boldsymbol{G}^l_{\boldsymbol{\phi}}(\boldsymbol{x}, \boldsymbol{Z}_{1:l-1})$
Codebook $\boldsymbol{B}_l$
b_1^l
b_K^l
Quantization
$\boldsymbol{Z}_l \sim \hat{P}_{s_l^2}(\boldsymbol{Z}_l|\tilde{\boldsymbol{Z}}_l)$
Prior distribution
$\mathcal{P}(\boldsymbol{Z}_l, \tilde{\boldsymbol{Z}}_l)$
$:= \prod_{i=1}^{d_l} P(\boldsymbol{z}_{l,i}) p_{s_l^2}(\tilde{\boldsymbol{z}}_{l,i}|\boldsymbol{Z}_l)$
Output (input to next layer)

(c) *Injected top-down* layer.

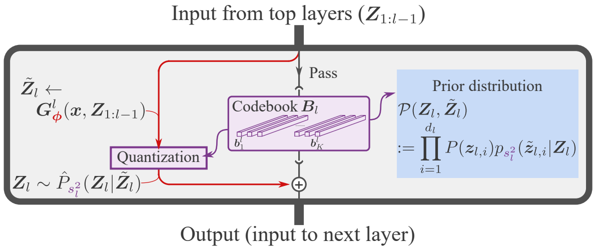
Input from top layers ($\boldsymbol{Z}_{1:l-1}$)
Pass
$\tilde{\boldsymbol{Z}}_l \leftarrow$
$\boldsymbol{G}^l_{\boldsymbol{\phi}}(\boldsymbol{x}, \boldsymbol{Z}_{1:l-1})$
Codebook $\boldsymbol{B}_l$
b_1^l
b_K^l
Quantization
$\boldsymbol{Z}_l \sim \hat{P}_{s_l^2}(\boldsymbol{Z}_l|\tilde{\boldsymbol{Z}}_l)$
Prior distribution
$\mathcal{P}(\boldsymbol{Z}_l, \tilde{\boldsymbol{Z}}_l)$
$:= \prod_{i=1}^{d_l} P(\boldsymbol{z}_{l,i}) p_{s_l^2}(\tilde{\boldsymbol{z}}_{l,i}|\boldsymbol{Z}_l)$
Output (input to next layer)

(d) *Residual top-down* layer.

Figure 1: (a) HQ-VAE consists of *bottom-up* and *top-down* paths. Red arrows are for approximated posterior. Kullback–Leibler divergence of posterior and prior (in the blue box) is evaluated for objective function. (b) First layer for *top-down* path. (c)-(d) We introduce two types of layers: *injected top-down* and *residual top-down*. HQ-VAE that consists only of the injected (residual) *top-down* layer is analogous to VQ-VAE-2 (RQ-VAE).

from $\boldsymbol{x}$ as $\boldsymbol{H}_{\boldsymbol{\phi}}^{r}(\boldsymbol{x})$ at different resolutions ($r \in [R]$). In the *top-down* path, the latent variable in each group is processed in the order from $\boldsymbol{Z}_1$ to $\boldsymbol{Z}_L$ by taking $\boldsymbol{H}_{\boldsymbol{\phi}}^{r}(\boldsymbol{x})$ into account. To achieve this, two features including that extracted by the *bottom-up* path ($\boldsymbol{H}_{\boldsymbol{\phi}}^{r}(\boldsymbol{x})$) and that processed at higher layers in the *top-down* path ($\boldsymbol{Z}_{1:l-1}$) can be fed to each layer and processed to estimate $\boldsymbol{Z}_l$ corresponding to $\boldsymbol{x}$, which we denote it as $\hat{\boldsymbol{Z}}_l = \boldsymbol{G}_{\boldsymbol{\phi}}^{l}(\boldsymbol{H}_{\boldsymbol{\phi}}^{r}(\boldsymbol{x}), \boldsymbol{Z}_{1:l-1})$. The lth group $\boldsymbol{Z}_l$ has a unique resolution index r, and we denote it as $r(l)$. For simplicity, we ignore $\boldsymbol{H}_{\boldsymbol{\phi}}^{r}$ in $\hat{\boldsymbol{Z}}_l$ and write $\hat{\boldsymbol{Z}}_l = \boldsymbol{G}_{\boldsymbol{\phi}}^{l}(\boldsymbol{x}, \boldsymbol{Z}_{1:l-1})$. The design of the encoding function $\boldsymbol{G}_{\boldsymbol{\phi}}^{l}$ brings us to different modeling of the approximated posterior. We leave the detailed discussion in the next section.

It should be noted that the outputs of $\boldsymbol{G}_{\boldsymbol{\phi}}^{l}$ lie in $\mathbb{R}^{d_z \times d_b}$, whereas the support of $\boldsymbol{Z}_l$ is restricted to $\boldsymbol{B}_l^{d_z}$. To connect these continuous and discrete spaces, we introduce a pair of stochastic dequantization and quantization processes, as in Takida et al. (2022b). We first define the stochastic dequantization process for each group as

$$p_{s_l^2}(\tilde{\boldsymbol{z}}_{l,i}|\boldsymbol{Z}_l) = \mathcal{N}(\tilde{\boldsymbol{z}}_{l,i}; \boldsymbol{z}_{l,i}, s_l^2\boldsymbol{I}), \tag{2}$$

which is equivalent to adding Gaussian noise to the discrete variable the covariance of which, $s_l^2\boldsymbol{I}$, depends on the index of the group l. We hereafter denote the set of $\tilde{\boldsymbol{Z}}_l$ as $\tilde{\boldsymbol{Z}}_{1:L}$, i.e., $\tilde{\boldsymbol{Z}}_{1:L} := \{\tilde{\boldsymbol{Z}}_l\}_{l=1}^{L}$. Next, we can derive a stochastic quantization process as the inverse operator of the above stochastic dequantization:

$$\hat{P}_{s_l^2}(\boldsymbol{z}_{l,i} = \boldsymbol{b}_k|\tilde{\boldsymbol{Z}}_l) \propto \exp\left(-\frac{\|\tilde{\boldsymbol{z}}_{l,i} - \boldsymbol{b}_k\|_2^2}{2s_l^2}\right). \tag{3}$$

By using these stochastic operators, we can connect $\hat{\boldsymbol{Z}}_{1:L}$ and $\boldsymbol{Z}_{1:L}$ via $\tilde{\boldsymbol{Z}}_{1:L}$ in a stochastic manner, which leads to the entire encoding process:

$$\mathcal{Q}(\boldsymbol{Z}_{1:L}, \tilde{\boldsymbol{Z}}_{1:L}|\boldsymbol{x}) = \prod_{l=1}^{L}\prod_{i=1}^{d_l} p_{s_l^2}(\tilde{\boldsymbol{z}}_{l,i}|\boldsymbol{G}_{\boldsymbol{\phi}}^{l}(\boldsymbol{x}, \boldsymbol{Z}_{1:l-1}))\hat{P}_{s_l^2}(\boldsymbol{z}_{l,i}|\tilde{\boldsymbol{Z}}_l). \tag{4}$$

The prior distribution on $\boldsymbol{Z}_{1:L}$ and $\tilde{\boldsymbol{Z}}_{1:L}$ is defined using the stochastic dequantization process as

$$\mathcal{P}(\boldsymbol{Z}_{1:L}, \tilde{\boldsymbol{Z}}_{1:L}) = \prod_{l=1}^{L}\prod_{i=1}^{d_l} P(\boldsymbol{z}_{l,i})p_{s_l^2}(\tilde{\boldsymbol{z}}_i|\boldsymbol{Z}_l), \tag{5}$$

where the latent representations are generated in the order from $l = 1$ to L. The generative process from the prior does not use $\tilde{\boldsymbol{Z}}$ but $\boldsymbol{Z}$ as $\boldsymbol{x} = \boldsymbol{f}_{\boldsymbol{\theta}}(\boldsymbol{Z})$.

4 Instantiations of HQ-VAE

Now that we have established the overall framework of HQ-VAE, we consider two special cases of HQ-VAE by designing two types of *top-down* layers: *injected top-down* and *residual top-down.* We derive two instances of HQ-VAE that consists only of the *injected top-down* layer or the *residual top-down* layer, which we call SQ-VAE-2 and RSQ-VAE, respectively due to their analogue to VQ-VAE-2 and RQ-VAE. These two layers can be combinatorially used to define a hybrid model of SQ-VAE-2 and RSQ-VAE, which is explained in Appendix B. Note that the prior distribution (Equation (5)) is identical across all instantiations.

4.1 First top-down layer

We introduce the first *top-down* layer, which is put at the top of layers in HQ-VAE. As illustrated in Figure 1b, this layer takes $\boldsymbol{H}_{\boldsymbol{\phi}}^{1}(\boldsymbol{x})$ as an input and processes it with SQ. HQ-VAE constructed only with this layer reduces to SQ-VAE.

4.2 Injected top-down layer

We design an *injected top-down* layer for the approximated posterior as in Figure 1c. This layer infuses the variable processed in the *top-down* path with the higher resolution information from the *bottom-up* layer. The lth layer takes the feature from the *bottom-up* path ($\boldsymbol{H}_{\boldsymbol{\phi}}^{r(l)}(\boldsymbol{x})$) and the variable from the higher groups in the *top-down* path as inputs. In the layer, the variable from higher layers is first upsampled to be aligned with $\boldsymbol{H}_{\boldsymbol{\phi}}^{r(l)}(\boldsymbol{x})$. These two variables are then concatenated and processed with an encoding block. The above overall process corresponds to $\hat{\boldsymbol{Z}}_l = \boldsymbol{G}_{\boldsymbol{\phi}}^{l}(\boldsymbol{x}, \boldsymbol{Z}_{1:l-1})$ in Section 3. The encoded variable $\hat{\boldsymbol{Z}}_l$ is then quantized into $\boldsymbol{Z}_l$ with the codebook $\boldsymbol{B}_l$ through the process described in Equation (3)[1]. Finally, the sum of the variable from the top layers and quantized variable $\boldsymbol{Z}_l$ is passed through to the next layer.

4.2.1 SQ-VAE-2

We especially instantiate the HQ-VAE only with the *injected top-down* layers in addition to the first layer, which reduces to SQ-VAE-2. Note that since the index of resolutions and layers have a one-to-one correspondence in this structure, $r(l) = l$ and $L = R$. As in usual VAEs, we evaluate the ELBO as $\log p_{\boldsymbol{\theta}}(\boldsymbol{x}) \geq -\mathcal{J}_{\text{SQ-VAE-2}}(\boldsymbol{x}; \boldsymbol{\theta}, \boldsymbol{\phi}, \boldsymbol{s}^2, \mathcal{B})$, where $\boldsymbol{s}^2 := \{s_l^2\}_{l=1}^{L}$, $\mathcal{B} := (\boldsymbol{B}_1, \cdots, \boldsymbol{B}_L)$ and

$$\mathcal{J}_{\text{SQ-VAE-2}}(\boldsymbol{x}; \boldsymbol{\theta}, \boldsymbol{\phi}, \boldsymbol{s}^2, \mathcal{B}) = \mathbb{E}_{\mathcal{Q}(\boldsymbol{Z}_{1:L}, \tilde{\boldsymbol{Z}}_{1:L}|\boldsymbol{x})}\left[-\log p_{\boldsymbol{\theta}}(\boldsymbol{x}|\boldsymbol{Z}_{1:L}) + \log \frac{\mathcal{Q}(\boldsymbol{Z}_{1:L}, \tilde{\boldsymbol{Z}}_{1:L}|\boldsymbol{x})}{\mathcal{P}(\boldsymbol{Z}_{1:L}, \tilde{\boldsymbol{Z}}_{1:L})}\right] \tag{6}$$

Hereafter, we omit the arguments of objective functions for simplicity. By decomposing $\mathcal{Q}$ and $\mathcal{P}$ and substituting parameterizations for the probabilistic parts, we have

$$\mathcal{J}_{\text{SQ-VAE-2}} = \frac{D}{2}\log\sigma^2 + \mathbb{E}_{\mathcal{Q}(\boldsymbol{Z}_{1:L}, \tilde{\boldsymbol{Z}}_{1:L}|\boldsymbol{x})}\left[\frac{\|\boldsymbol{x} - f_{\boldsymbol{\theta}}(\boldsymbol{Z}_{1:L})\|_2^2}{2\sigma^2} + \sum_{l=1}^{L}\left(\frac{\|\tilde{\boldsymbol{Z}}_l - \boldsymbol{Z}_l\|_F^2}{2s_l^2} - H(\hat{P}_{s_l^2}(\boldsymbol{Z}_l|\tilde{\boldsymbol{Z}}_l))\right)\right], \tag{7}$$

where $H(\cdot)$ indicates the entropy of a probability mass function and constant terms are omitted. The derivation of Equation (7) is given in Appendix A. The objective function (7) consists of the reconstruction term and the regularization terms for $\boldsymbol{Z}_{1:L}$ and $\tilde{\boldsymbol{Z}}_{1:L}$. The expectation w.r.t. the probability mass function $\hat{P}_{s_l^2}(\boldsymbol{z}_{l,i} = \boldsymbol{b}_k|\tilde{\boldsymbol{Z}}_l)$ can be approximated with the corresponding Gumbel-softmax distribution Maddison et al. (2017); Jang et al. (2017) in a reparameterizable manner.

4.2.2 SQ-VAE-2 vs. VQ-VAE-2

The architecture of VQ-VAE-2 is composed in a similar fashion to that of SQ-VAE-2 but is trained by the following objective function:

$$\mathcal{L}_{\text{VQ-VAE-2}} = \|\boldsymbol{x} - \boldsymbol{f}_{\boldsymbol{\theta}}(\boldsymbol{Z}_{1:L})\|_2^2 + \beta\sum_{l=1}^{L}\|\boldsymbol{G}_{\boldsymbol{\phi}}^{l}(\boldsymbol{x}, \boldsymbol{Z}_{1:l-1}) - \text{sg}[\boldsymbol{Z}_l]\|_F^2, \tag{8}$$

where the codebooks are updated with the EMA update in the same manner as the original VQ-VAE. The objective function (8), except for the stop gradient operator and EMA update, can be obtained by setting both s_l^2 and σ^2 to infinity while keeping the ratio of the variances as $s_l^2 = \beta^{-1}\sigma^2$ for $l \in [L]$ in Equation (7). In contrast, since all the parameters but D and L in Equation (7) are optimized, the weight of each term is automatically adjusted during training. Furthermore, SQ-VAE-2 is expected to benefit from the *self-annealing* effect as in the original SQ-VAE (see Section 5.3).

4.3 Residual top-down layer

In this subsection, we set $R = 1$ for the simplicity of the demonstration purpose (general case of R is in Appendix B). This means the *bottom-up* and *top-down* paths are connected only at the top layer. We design

---

[1] We empirically found setting $\tilde{\boldsymbol{Z}}_l$ to $\hat{\boldsymbol{Z}}_l$ instead of sampling $\tilde{\boldsymbol{Z}}_l$ from $p_{\boldsymbol{s}^2}(\tilde{z}_{l,i}|\hat{\boldsymbol{Z}}_l)$ leads to better performance (as reported in Takida et al. (2022b); therefore, we follow the procedure in practice.

a *residual top-down* layer for the approximated posterior as in Figure 1d. This layer is to better approximate the target feature with additional assignments of code vectors. By stacking this procedure L times, the feature is approximated as

$$\boldsymbol{H}_{\boldsymbol{\phi}}(\boldsymbol{x}) \approx \sum_{l=1}^{L} \boldsymbol{Z}_l. \tag{9}$$

Therefore, in this layer, only the information from the higher layers but from the *bottom-up* path is fed to the layer. It is desired that $\sum_{l'=1}^{l+1} \boldsymbol{Z}_{l'}$ approximate the feature better than $\sum_{l'=1}^{l} \boldsymbol{Z}_{l'}$. On this basis, we let the following residual pass through to the next layer:

$$\boldsymbol{G}^{l}_{\boldsymbol{\phi}}(\boldsymbol{x}, \boldsymbol{Z}_{1:l-1}) = \boldsymbol{H}_{\boldsymbol{\phi}}(\boldsymbol{x}) - \sum_{l=1}^{l-1} \boldsymbol{Z}_{l'}. \tag{10}$$

4.3.1 RSQ-VAE

We especially instantiate the HQ-VAE only with the *residual top-down* layers in addition to the first layer, which reduces to RSQ-VAE. At this point, by following Equation (6) and omitting constant terms, we can derive the same form of the ELBO objective as Equation (7):

$$\mathcal{J}^{\text{naïve}}_{\text{RSQ-VAE}} = \frac{D}{2}\log\sigma^2 + \mathbb{E}_{\mathcal{Q}(\boldsymbol{Z}_{1:L}, \tilde{\boldsymbol{Z}}_{1:L}|\boldsymbol{x})}\left[\frac{\|\boldsymbol{x} - \boldsymbol{f}_{\boldsymbol{\theta}}(\boldsymbol{Z}_{1:L})\|_2^2}{2\sigma^2} + \sum_{l=1}^{L}\left(\frac{\|\tilde{\boldsymbol{Z}}_l - \boldsymbol{Z}_l\|_F^2}{2s_l^2} - H(\hat{P}_{s_l^2}(\boldsymbol{Z}_l|\tilde{\boldsymbol{Z}}_l))\right)\right], \tag{11}$$

where the numerator of the third term corresponds to the evaluation of the residuals $\boldsymbol{H}_{\boldsymbol{\phi}}(\boldsymbol{x}) - \sum_{l'=1}^{l} \boldsymbol{Z}_{l'}$ for all $l \in [L]$ with the dequantization process. However, we empirically found training the model with the ELBO objective was often unstable. We suspect this is because the objective regularizes $\boldsymbol{Z}_{1:L}$ to make $\sum_{l'=1}^{l} \boldsymbol{Z}_{l'}$ close to the feature for all $l \in [L]$. We hypothesize that this regularization is too strong to regularize the latent representation. To address the issue, we consider conditional distributions not on $(\boldsymbol{Z}_{1:L}, \tilde{\boldsymbol{Z}}_{1:L})$ but on $(\boldsymbol{Z}_{1:L}, \tilde{\boldsymbol{Z}})$, where $\tilde{\boldsymbol{Z}} = \sum_{l=1}^{L} \tilde{\boldsymbol{Z}}_l$. From the reproductive property of Gaussian distribution, the continuous latent variable converted from $\boldsymbol{Z}$ via the stochastic dequantization processes, $\tilde{\boldsymbol{Z}} = \sum_{l=1}^{L} \tilde{\boldsymbol{Z}}_l$, follows the following Gaussian distribution:

$$p_{\boldsymbol{s}^2}(\tilde{\boldsymbol{z}}_i|\boldsymbol{Z}) = \mathcal{N}\left(\tilde{\boldsymbol{z}}_i; \sum_{l=1}^{L} \boldsymbol{z}_{l,i}, \left(\sum_{l=1}^{L} s_l^2\right)\boldsymbol{I}\right). \tag{12}$$

We instead use the following prior distribution to derive the ELBO objective:

$$\mathcal{P}(\boldsymbol{Z}_{1:L}, \tilde{\boldsymbol{Z}}) = \prod_{i=1}^{d_z}\left(\prod_{l=1}^{L} P(\boldsymbol{z}_{l,i})\right) p_{\boldsymbol{s}^2}(\tilde{\boldsymbol{z}}_i|\boldsymbol{Z}). \tag{13}$$

We now derive the ELBO using the newly established prior and posterior starting from

$$\begin{aligned}\log p_{\boldsymbol{\theta}}(\boldsymbol{x}) &\geq -\mathcal{J}_{\text{RSQ-VAE}} \\ &= -\mathbb{E}_{\mathcal{Q}(\boldsymbol{Z}_{1:L}, \tilde{\boldsymbol{Z}}|\boldsymbol{x})}\left[-\log p_{\boldsymbol{\theta}}(\boldsymbol{x}|\boldsymbol{Z}_{1:L}) + \log\frac{\mathcal{Q}(\boldsymbol{Z}_{1:L}, \tilde{\boldsymbol{Z}}|\boldsymbol{x})}{\mathcal{P}(\boldsymbol{Z}_{1:L}, \tilde{\boldsymbol{Z}})}\right].\end{aligned} \tag{14}$$

The above objective is further simplified as

$$\mathcal{J}_{\text{RSQ-VAE}} = \frac{D}{2}\log\sigma^2 + \mathbb{E}_{\mathcal{Q}(\boldsymbol{Z}_{1:L}, \tilde{\boldsymbol{Z}}_{1:L}|\boldsymbol{x})}\left[\frac{\|\boldsymbol{x} - \boldsymbol{f}_{\boldsymbol{\theta}}(\boldsymbol{Z}_{1:L})\|_2^2}{2\sigma^2} + \frac{\|\tilde{\boldsymbol{Z}} - \boldsymbol{Z}\|_F^2}{2\sum_{l=1}^{L} s_l^2} - \sum_{l=1}^{L} H(\hat{P}_{s_l^2}(\boldsymbol{Z}_l|\tilde{\boldsymbol{Z}}_l))\right] \tag{15}$$

where the third term is different from that in Equation (11) and its numerator evaluates only the overall quantization error $\boldsymbol{H}_{\boldsymbol{\phi}}(\boldsymbol{x}) - \sum_{l=1}^{L} \boldsymbol{Z}_l$ with the dequantization process.

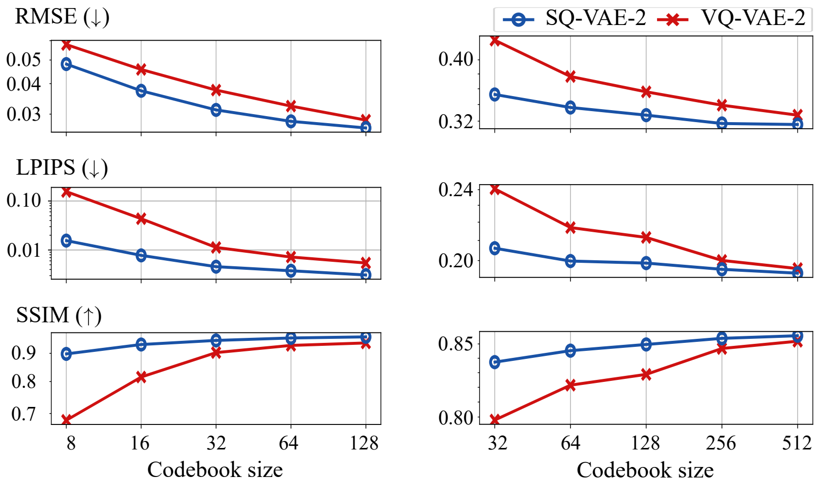

(a) CIFAR10 (b) CelebA-HQ

Figure 2: Impact of codebook capacity on reconstruction is investigated on (a) CIFAR10 and (b) CelebA-HQ. Two and three layers are tested on CIFAR10 and CelebA-HQ, respectively.

Table 1: Evaluation on ImageNet (256×256) and FFHQ (1024×1024). RMSE ($\times 10^2$), LPIPS, and SSIM are evaluated using test set. Following Razavi et al. (2019), codebook capacity for discrete latent space is set to $(d_l, K_l) = (32^2, 512), (64^2, 512)$ and $(d_l, K_l) = (32^2, 512), (64^2, 512), (128^2, 512)$ for ImageNet and FFHQ, respectively. We also show codebook perplexity at each layer.

Dataset	Model	Reconstruction			Codebook perplexity		
		RMSE ↓	LPIPS ↓	SSIM ↑	$\boldsymbol{Z}_1$	$\boldsymbol{Z}_2$	$\boldsymbol{Z}_3$
ImageNet	VQ-VAE-2	6.071 ± 0.006	0.265 ± 0.012	0.751 ± 0.000	106.8 ± 0.8	288.8 ± 1.4	
	SQ-VAE-2	4.603 ± 0.006	0.096 ± 0.000	0.855 ± 0.006	406.2 ± 0.9	355.5 ± 1.7	
FFHQ	VQ-VAE-2	4.866 ± 0.291	0.323 ± 0.012	0.814 ± 0.003	24.6 ± 10.7	41.3 ± 14.0	310.1 ± 29.6
	SQ-VAE-2	2.118 ± 0.013	0.166 ± 0.002	0.909 ± 0.001	125.8 ± 9.0	398.7 ± 14.1	441.3 ± 7.9

4.3.2 RSQ-VAE vs. RQ-VAE

RQ-VAE and RSQ-VAE both learn discrete representation in a coarse-to-fine manner, but RQ-VAE adopts a deterministic RQ scheme to achieve Equation (9), where RQ-VAE is trained with the following objective function:

$$\mathcal{L}_{\text{RQ-VAE}} = \|\boldsymbol{x} - \boldsymbol{f}_{\boldsymbol{\theta}}(\boldsymbol{Z}_{1:L})\|_2^2 + \beta \sum_{l=1}^{L} \left\| \boldsymbol{H}_{\boldsymbol{\phi}}(\boldsymbol{x}) - \mathrm{sg}\left[\sum_{l'=1}^{l} \boldsymbol{Z}_{l'} \right] \right\|_F^2, \tag{16}$$

where the codebooks are updated with the EMA update in the same manner as VQ-VAE. The second term of Equation (16) resembles the third term of Equation (11), which strongly enforces certain degree of reconstruction even only with partial information from the higher layers. RQ-VAE is beneficial from such a regularization term, which leads to stable training. However, in RSQ-VAE, this regularization deteriorates the reconstruction performance. Instead, we use Equation (15) as the objective, which regularizes the latent representation by taking into account only accumulated information from all layers.

Remark. HQ-VAE has favorable properties similar to SQ-VAE. The training scheme does not require hyperparameters except for a temperature parameter of Gumbel-softmax approximation (see Equations (7) and (15)). Furthermore, the derived models can benefit from the *self-annealing effect* as in SQ-VAE, which is empirically shown in Section 5.3.

5 Experiments

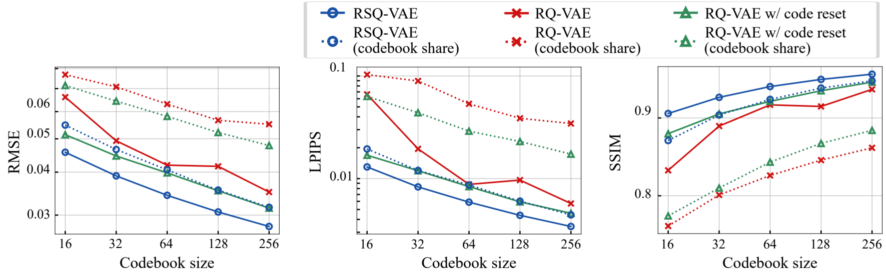

(a) CIFAR10 ($L = 4$)

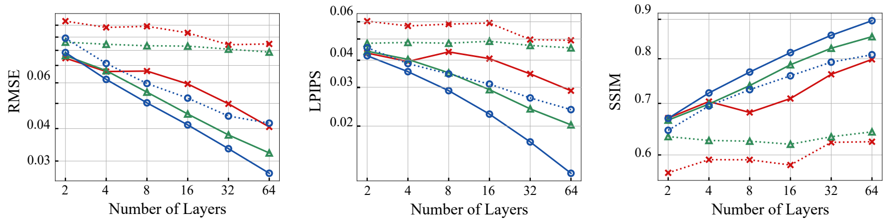

(b) CelebA-HQ ($K_l = 32$)

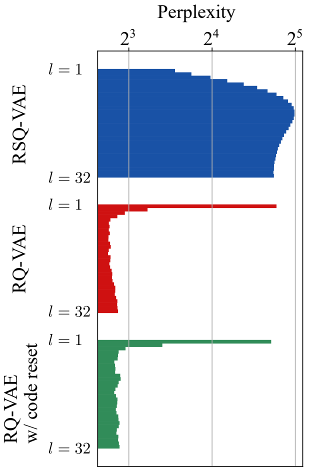

(c) Codebook perplexity.

Figure 3: Impact of codebook capacity on reconstruction is investigated on (a) CIFAR10 and (b) CelebA-HQ. (c) Codebook perplexity at each layer is plotted, wheremodels with 32 layers are trained on CelebA-HQ and all layers share same codebook.

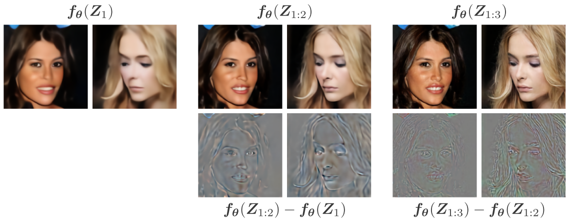
$f_\theta(Z_1)$
$f_\theta(Z_{1:2})$
$f_\theta(Z_{1:3})$
$f_\theta(Z_{1:2}) - f_\theta(Z_1)$
$f_\theta(Z_{1:3}) - f_\theta(Z_{1:2})$

(a) Reconstructed images and magnified differences of SQ-VAE-2

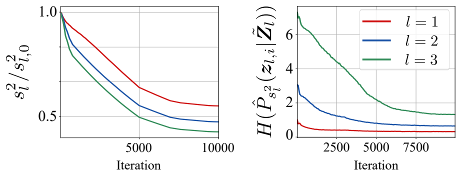

(b) $H(\hat{P}_{s_l^2}(\boldsymbol{z}_{l,i}|\tilde{\boldsymbol{Z}}_l))$ in SQ-VAE-2

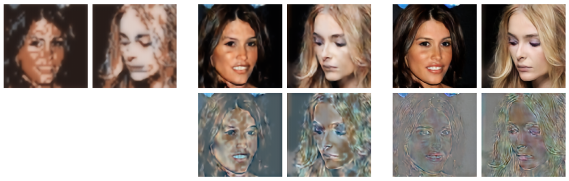

(c) Reconstructed images and magnified differences of RSQ-VAE

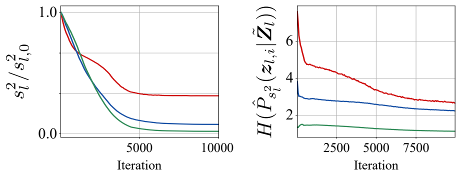

(d) $H(\hat{P}_{s_l^2}(\boldsymbol{z}_{l,i}|\tilde{\boldsymbol{Z}}_l))$ in RSQ-VAE

Figure 4: Reconstructed samples with partial layers in (a) SQ-VAE-2 and (c) RSQ-VAE. Top row shows reconstructed images while bottom one shows added components at each layer. For $l = 1, 2, 3$ latent capacity is set to $(d_l, K_l) = (16^2, 256), (32^2, 16), (64^2, 4)$ and $(d_l, K_l) = (32^2, 4), (32^2, 16), (32^2, 256)$, respectively. Notice that the numbers of bits of these models are equal at each layer. For reasonable visualization, we apply *progressive coding* to SQ-VAE-2, which induces progressive compression (see Appendix C.5). (b) and (d) We plot variance parameter s_l^2 normalized by initial value $s_{l,0}^2$ and average entropy of quantization process $(H(\hat{P}_{s_l^2}(\boldsymbol{z}_{l,i}|\tilde{\boldsymbol{Z}}_l)))$ at each layer.

We comprehensively examine SQ-VAE-2 and RSQ-VAE and visualize the effects of their individual *top-down* paths. In Secs. 5.1 and 5.2, we comprehensively compare SQ-VAE-2 and RSQ-VAE with VQ-VAE-2 and RQ-VAE, respectively to show our framework improves reconstruction performance against the baselines. In addition, we show that RSQ-VAE trained with a perceptual loss Johnson et al. (2016) is competitive with the state-of-the-art model based on RQ-VAE. Furthermore, we test HQ-VAE on an audio dataset to show that it is applicable to a different modality. In Section 5.3, we investigate the characteristics of the *injected top-down* and *residual top-down* layers with visualization (Section 5.3). Unless otherwise noted, we use the same network architecture in all models and set the codebook dimension to $d_b = 64$. The experimental details are given in Appendix C.

5.1 SQ-VAE-2 vs. VQ-VAE-2

We compare SQ-VAE-2 with VQ-VAE-2 from the aspects of reconstruction accuracy and codebook utilization. We first investigate their performance on CIFAR10 Krizhevsky et al. (2009) and CelebA-HQ (256×256) in various codebook settings: the configurations for the hierarchical structure and numbers of code vectors (K_l). We evaluated the reconstruction accuracy in terms of the root mean squared error (RMSE), structure similarity index (SSIM) Wang et al. (2004), and learned perceptual image patch similarity (LPIPS) Zhang et al. (2018). As shown in Figure 2, SQ-VAE-2 achieved better reconstruction accuracy in all cases. The difference of the performance between the two models is noticeable when the codebook size is small.

Comparison on large-scale datasets. Next, we demonstrate that SQ-VAE-2 outperforms VQ-VAE-2 on ImageNet (256×256) Deng et al. (2009) and FFHQ (1024×1024) Karras et al. (2019) in the same latent settings as in Razavi et al. (2019). As shown in Table 1, SQ-VAE-2 achieves better reconstruction performance in terms of RMSE, LPIPS, and SSIM than VQ-VAE-2, which is a similar tendency as in the comparison on CIFAR10 and CelebA-HQ. Furthermore, we measure codebook utilization by the perplexity of latent variables. SQ-VAE-2 achieves higher codebook perplexities than VQ-VAE-2 at all the layers, whereas the higher layers are not effectively used in VQ-VAE-2.

5.2 RSQ-VAE vs. RQ-VAE

We compare RSQ-VAE with RQ-VAE using the same metrics as in Section 5.1. As codebook reset is used in the original study Zeghidour et al. (2021); Lee et al. (2022a), we added VQ-VAE with this technique to the baselines. We first investigate their performances on CIFAR10 and CelebA-HQ (256×256) in various settings: the number of times of quantization step (l) and number of code vectors (K_l). As shown in Figures 3a and 3b, RSQ-VAE achieves better reconstruction accuracy in terms of RMSE, SSIM, and LPIPS than the baselines although codebook reset overall enhances the performance of RQ-VAE. When the codebook is shared for all layers, the performance difference is remarkable, with a noticeable difference in how codes are used. Interestingly, more codes are assigned in the bottom layers in RSQ-VAE, unlike RQ-VAEs, as shown in Figure 3c. RSQ-VAE captures the coarse information with a relatively small number of codes, and refines the reconstruction with larger bits at the bottom layers.

Improvement in perceptual quality. Next, we use the same network architecture as that used in Lee et al. (2022a) and set the codebook dimension to $d_b = 256$ for fair comparison with their RQ-VAE. We train RSQ-VAE on FFHQ with an LPIPS loss Zhang et al. (2018) (see Appendix C.4) and compare it with their RQ-VAE in terms of Fréchet Inception Distance (FID) Heusel et al. (2017). The reconstructed FID (rFID) of RSQ-VAE is 8.47, whereas that of their RQ-VAE is 7.29. Note that we do not use an adversarial loss for training RSQ-VAE but their RQ-VAE was trained with the combination of an LPIPS loss and adversarial loss. This means that our RSQ-VAE achieves competitive performance without an adversarial loss. We leave combining an adversarial loss with HQ-VAE for future work.

Validation on an audio dataset. To validate the effectiveness of RSQ-VAE in the audio domain, we compare it with RQ-VAE by the reconstruction of the normalized log-Mel spectrogram using an environmental sound dataset: UrbanSound8K Salamon et al. (2014). We follow the same network architecture used in an audio generation paper Liu et al. (2021), which deploys multi-scale convolutional layers with varied

Table 2: Evaluation on UrbanSound8K. RMSE is evaluated using test set. Network architecture follows Liu et al. (2021). Codebook size is set to $K_l = 8$.

Model	Number of Layers	RMSE ↓
RQ-VAE	4	0.506 ± 0.018
	8	0.497 ± 0.057
RSQ-VAE	4	0.427 ± 0.014
	8	0.314 ± 0.013

kernel sizes to capture the local and global features of audio signals in the time-frequency domain Xian et al. (2021). Codebook size is set to $K_l = 8$. Number of layers is set to 4 and 8, and all the layers share the same codebook. We run each trial with five different random seeds and obtain the average and standard deviation of RMSEs. As shown in Table 2, RSQ-VAE achieves better average RMSEs than RQ-VAE across different numbers of layers on the audio dataset.

5.3 Empirical study of top-down layers

In this section, we focus on visualizing the obtained discrete representations instead of comparing their reconstruction performance. This will provide insights into the characteristics of the *top-down* layers. We train both, SQ-VAE-2 and RSQ-VAE, with three layers on CelebA-HQ Karras et al. (2018), respectively. Figure 4 shows the progressively reconstructed images. For demonstration purpose, we incorporate *progressive coding* Shu & Ermon (2022) to SQ-VAE-2 to make the reconstructed images only with the top layers interpretable. We note that *progressive coding* is not applied other than the illustration of Figure 4. Both, SQ-VAE-2 and RSQ-VAE, share the similarity that the higher layers generate the coarse part of the image while the lower layers complement them with details. However, comparing the two, we observe that in SQ-VAE-2, the additionally generated components (bottom row in Figure 4a) in each layer have different resolutions. We conjecture that the different layer-dependent resolutions $\boldsymbol{H}_{\boldsymbol{\phi}}^{r(l)}(\boldsymbol{x})$, which are injected into the *top-down* layers, contain different information. This implies that we may obtain more interpretable discrete representations if we can explicitly manipulate the extracted features in the *bottom-up* path to provide $\boldsymbol{H}_{\boldsymbol{\phi}}^{r(l)}(\boldsymbol{x})$ giving them more semantic meaning (e.g., texture or color). In contrast, RSQ-VAE seems to obtain a different discrete representation which resembles more a decomposition. This might be due to its approximated expansion in Equation (9). Moreover, we can observe from Figures 4b and 4d that the *top-down* layers also benefit from the *self-annealing* effect.

In Appendix C.3, we explore combining the two layers to form a hybrid model. We observe that individual layers in a hybrid model produce similar effects as if they would be used alone. That is, outputs from *injected top-down* layers have better resolution and *residual top-down* layers refine upon certain decomposition. Since these two layers enjoy distinct refining mechanisms, a hybrid model may bring a more flexible approximation to the posterior distribution.

6 Conclusion

We propose HQ-VAE, a general VAE approach that learns hierarchical discrete representations. HQ-VAE is formulated within the variational Bayes framework as a stochastic quantization technique, which (1) greatly reduces the number of hyperparameters to be tuned (only the one from the Gumbel-softmax trick), and (2) enhances codebook usage without any heuristics thanks to the *self-annealing* effect. We instantiate the general HQ-VAE with two types of posterior approximators for the discrete latent representations, which lead to SQ-VAE-2 and RSQ-VAE. These two novel variants share a similar design of information passing as VQ-VAE-2 and RQ-VAE, respectively, but their latent representations are quantized stochastically. Our experiments show that SQ-VAE-2 and RSQ-VAE outperform their individual baselines with better reconstruction and more efficient codebook usages in the image as well as audio domain.

As future work, we will incorporate adversarial training into HQ-VAE which is expected to further enhance the perceptual quality of the reconstructed data. As discussed in Section 5.3, we will also explore the feasibility of explicitly manipulating the injected information into the *top-down* layers to obtain discrete representations with semantic meaning. At last, we explore one of the applications to image generation by training a prior on extracted discrete representations with HQ-VAE in Section D. Nevertheless, this work is focusing on providing a unified variational Bayesian framework of hierarchical quantization. Its downstream applications such as content generation or neural codec will also be considered as future work.

References

Eirikur Agustsson, Fabian Mentzer, Michael Tschannen, Lukas Cavigelli, Radu Timofte, Luca Benini, and Luc V Gool. Soft-to-hard vector quantization for end-to-end learning compressible representations. In *Proc. Advances in Neural Information Processing Systems (NeurIPS)*, 2017.

Jacob Austin, Daniel D Johnson, Jonathan Ho, Daniel Tarlow, and Rianne van den Berg. Structured denoising diffusion models in discrete state-spaces. In *Proc. Advances in Neural Information Processing Systems (NeurIPS)*, volume 34, pp. 17981–17993, 2021.

Xi Chen, Nikhil Mishra, Mostafa Rohaninejad, and Pieter Abbeel. Pixelsnail: An improved autoregressive generative model. In *Proc. International Conference on Machine Learning (ICML)*, pp. 864–872. PMLR, 2018.

Rewon Child. Very deep VAEs generalize autoregressive models and can outperform them on images. In *Proc. International Conference on Learning Representation (ICLR)*, 2021.

Rewon Child, Scott Gray, Alec Radford, and Ilya Sutskever. Generating long sequences with sparse transformers. *arXiv preprint arXiv:1904.10509*, 2019.

Alexandre Défossez, Jade Copet, Gabriel Synnaeve, and Yossi Adi. High fidelity neural audio compression. *arXiv preprint arXiv:2210.13438*, 2022.

Jia Deng, Wei Dong, Richard Socher, Li-Jia Li, Kai Li, and Li Fei-Fei. Imagenet: A large-scale hierarchical image database. In *Proc. IEEE Conference on Computer Vision and Pattern Recognition (CVPR)*, pp. 248–255. Ieee, 2009.

Prafulla Dhariwal and Alexander Nichol. Diffusion models beat GANs on image synthesis. In *Proc. Advances in Neural Information Processing Systems (NeurIPS)*, volume 34, pp. 8780–8794, 2021.

Prafulla Dhariwal, Heewoo Jun, Christine Payne, Jong Wook Kim, Alec Radford, and Ilya Sutskever. Jukebox: A generative model for music. *arXiv preprint arXiv:2005.00341*, 2020.

Patrick Esser, Robin Rombach, Andreas Blattmann, and Bjorn Ommer. Imagebart: Bidirectional context with multinomial diffusion for autoregressive image synthesis. In *Proc. Advances in Neural Information Processing Systems (NeurIPS)*, volume 34, pp. 3518–3532, 2021a.

Patrick Esser, Robin Rombach, and Bjorn Ommer. Taming transformers for high-resolution image synthesis. In *Proc. IEEE/CVF Conference on Computer Vision and Pattern Recognition (CVPR)*, pp. 12873–12883, 2021b.

Shuyang Gu, Dong Chen, Jianmin Bao, Fang Wen, Bo Zhang, Dongdong Chen, Lu Yuan, and Baining Guo. Vector quantized diffusion model for text-to-image synthesis. In *Proc. IEEE/CVF Conference on Computer Vision and Pattern Recognition (CVPR)*, pp. 10696–10706, 2022.

Martin Heusel, Hubert Ramsauer, Thomas Unterthiner, Bernhard Nessler, and Sepp Hochreiter. GANs trained by a two time-scale update rule converge to a local Nash equilibrium. In *Proc. Advances in Neural Information Processing Systems (NeurIPS)*, pp. 6626–6637, 2017.

Jonathan Ho, Ajay Jain, and Pieter Abbeel. Denoising diffusion probabilistic models. In *Proc. Advances in Neural Information Processing Systems (NeurIPS)*, pp. 6840–6851, 2020.

Emiel Hoogeboom, Didrik Nielsen, Priyank Jaini, Patrick Forré, and Max Welling. Argmax flows and multinomial diffusion: Learning categorical distributions. In *Proc. Advances in Neural Information Processing Systems (NeurIPS)*, volume 34, pp. 12454–12465, 2021.

Eric Jang, Shixiang Gu, and Ben Poole. Categorical reparameterization with gumbel-softmax. In *Proc. International Conference on Learning Representation (ICLR)*, 2017.

Justin Johnson, Alexandre Alahi, and Li Fei-Fei. Perceptual losses for real-time style transfer and super-resolution. In *Proc. European Conference on Computer Vision (ECCV)*, pp. 694–711, 2016.

Lukasz Kaiser, Samy Bengio, Aurko Roy, Ashish Vaswani, Niki Parmar, Jakob Uszkoreit, and Noam Shazeer. Fast decoding in sequence models using discrete latent variables. In *Proc. International Conference on Machine Learning (ICML)*, pp. 2390–2399, 2018.

Tero Karras, Timo Aila, Samuli Laine, and Jaakko Lehtinen. Progressive growing of gans for improved quality, stability, and variation. In *Proc. International Conference on Learning Representation (ICLR)*, 2018.

Tero Karras, Samuli Laine, and Timo Aila. A style-based generator architecture for generative adversarial networks. In *Proc. IEEE/CVF Conference on Computer Vision and Pattern Recognition (CVPR)*, pp. 4401–4410, 2019.

Felix Kreuk, Gabriel Synnaeve, Adam Polyak, Uriel Singer, Alexandre Défossez, Jade Copet, Devi Parikh, Yaniv Taigman, and Yossi Adi. Audiogen: Textually guided audio generation. *arXiv preprint arXiv:2209.15352*, 2022.

Alex Krizhevsky, Geoffrey Hinton, et al. Learning multiple layers of features from tiny images. 2009.

Doyup Lee, Chiheon Kim, Saehoon Kim, Minsu Cho, and Wook-Shin Han. Autoregressive image generation using residual quantization. In *IEEE/CVF Conference on Computer Vision and Pattern Recognition (CVPR)*, pp. 11523–11532, 2022a.

Doyup Lee, Chiheon Kim, Saehoon Kim, Minsu Cho, and Wook-Shin Han. Draft-and-revise: Effective image generation with contextual rq-transformer. In *Proc. Advances in Neural Information Processing Systems (NeurIPS)*, 2022b.

Xubo Liu, Turab Iqbal, Jinzheng Zhao, Qiushi Huang, Mark D Plumbley, and Wenwu Wang. Conditional sound generation using neural discrete time-frequency representation learning. In *IEEE Int. Workshop on Machine Learning for Signal Processing (MLSP)*, pp. 1–6, 2021.

Chris J Maddison, Andriy Mnih, and Yee Why Teh. The concrete distribution: A continuous relaxation of discrete random variables. In *Proc. International Conference on Learning Representation (ICLR)*, 2017.

Boris T Polyak and Anatoli B Juditsky. Acceleration of stochastic approximation by averaging. *SIAM Journal on Control and Optimization*, 30(4):838–855, 1992.

Aditya Ramesh, Mikhail Pavlov, Gabriel Goh, Scott Gray, Chelsea Voss, Alec Radford, Mark Chen, and Ilya Sutskever. Zero-shot text-to-image generation. In *Proc. International Conference on Machine Learning (ICML)*, pp. 8821–8831, 2021.

Ali Razavi, Aaron van den Oord, and Oriol Vinyals. Generating diverse high-fidelity images with VQ-VAE-2. In *Proc. Advances in Neural Information Processing Systems (NeurIPS)*, pp. 14866–14876, 2019.

Robin Rombach, Andreas Blattmann, Dominik Lorenz, Patrick Esser, and Björn Ommer. High-resolution image synthesis with latent diffusion models. In *Proc. IEEE/CVF Conference on Computer Vision and Pattern Recognition (CVPR)*, pp. 10684–10695, 2022.

Aurko Roy, Ashish Vaswani, Arvind Neelakantan, and Niki Parmar. Theory and experiments on vector quantized autoencoders. *arXiv preprint arXiv:1805.11063*, 2018.

Justin Salamon, Christopher Jacoby, and Juan Pablo Bello. A dataset and taxonomy for urban sound research. In *ACM Int. Conf. on Multimedia (ACM MM)*, pp. 1041–1044, 2014.

Rui Shu and Stefano Ermon. Bit prioritization in variational autoencoders via progressive coding. In *International Conference on Machine Learning (ICML)*, pp. 20141–20155, 2022.

Jascha Sohl-Dickstein, Eric Weiss, Niru Maheswaranathan, and Surya Ganguli. Deep unsupervised learning using nonequilibrium thermodynamics. In *Proc. International Conference on Machine Learning (ICML)*, pp. 2256–2265. PMLR, 2015.

Casper Kaae Sønderby, Tapani Raiko, Lars Maaløe, Søren Kaae Sønderby, and Ole Winther. Ladder variational autoencoders. In *Proc. Advances in Neural Information Processing Systems (NeurIPS)*, pp. 3738–3746, 2016.

Jiaming Song, Chenlin Meng, and Stefano Ermon. Denoising diffusion implicit models. In *Proc. International Conference on Learning Representation (ICLR)*, 2020.

Yuhta Takida, Wei-Hsiang Liao, Chieh-Hsin Lai, Toshimitsu Uesaka, Shusuke Takahashi, and Yuki Mitsufuji. Preventing oversmoothing in VAE via generalized variance parameterization. *Neurocomputing*, 509:137–156, 2022a.

Yuhta Takida, Takashi Shibuya, WeiHsiang Liao, Chieh-Hsin Lai, Junki Ohmura, Toshimitsu Uesaka, Naoki Murata, Takahashi Shusuke, Toshiyuki Kumakura, and Yuki Mitsufuji. SQ-VAE: Variational bayes on discrete representation with self-annealed stochastic quantization. In *Proc. International Conference on Machine Learning (ICML)*, 2022b.

Lucas Theis, Wenzhe Shi, Andrew Cunningham, and Ferenc Huszár. Lossy image compression with compressive autoencoders. In *Proc. International Conference on Learning Representation (ICLR)*, 2017.

George Toderici, Sean M O'Malley, Sung Jin Hwang, Damien Vincent, David Minnen, Shumeet Baluja, Michele Covell, and Rahul Sukthankar. Variable rate image compression with recurrent neural networks. In *Proc. International Conference on Learning Representation (ICLR)*, 2016.

Arash Vahdat and Jan Kautz. Nvae: A deep hierarchical variational autoencoder. In *Proc. Advances in Neural Information Processing Systems (NeurIPS)*, volume 33, pp. 19667–19679, 2020.

Aäron van den Oord, Nal Kalchbrenner, and Koray Kavukcuoglu. Pixel recurrent neural networks. In *Proc. International Conference on Machine Learning (ICML)*, pp. 1747–1756, 2016.

Aäron van den Oord, Oriol Vinyals, and Koray Kavukcuoglu. Neural discrete representation learning. In *Proc. Advances in Neural Information Processing Systems (NeurIPS)*, pp. 6306–6315, 2017.

Dezhao Wang, Wenhan Yang, Yueyu Hu, and Jiaying Liu. Neural data-dependent transform for learned image compression. In *Proc. IEEE Conference on Computer Vision and Pattern Recognition (CVPR)*, pp. 17379–17388, 2022.

Zhou Wang, Alan C Bovik, Hamid R Sheikh, and Eero P Simoncelli. Image quality assessment: from error visibility to structural similarity. *IEEE transactions on image processing*, 13(4):600–612, 2004.

Will Williams, Sam Ringer, Tom Ash, John Hughes, David MacLeod, and Jamie Dougherty. Hierarchical quantized autoencoders. *arXiv preprint arXiv:2002.08111*, 2020.

Yang Xian, Yang Sun, Wenwu Wang, and Syed Mohsen Naqvi. Multi-scale residual convolutional encoder decoder with bidirectional long short-term memory for single channel speech enhancement. In *Proc. European Signal Process. Conf. (EUSIPCO)*, pp. 431–435, 2021.

Dongchao Yang, Jianwei Yu, Helin Wang, Wen Wang, Chao Weng, Yuexian Zou, and Dong Yu. Diffsound: Discrete diffusion model for text-to-sound generation. *arXiv preprint arXiv:2207.09983*, 2022.

Neil Zeghidour, Alejandro Luebs, Ahmed Omran, Jan Skoglund, and Marco Tagliasacchi. SoundStream: An end-to-end neural audio codec. *IEEE Trans. Audio, Speech, Lang. Process.*, 30:495–507, 2021.

Richard Zhang, Phillip Isola, Alexei A Efros, Eli Shechtman, and Oliver Wang. The unreasonable effectiveness of deep features as a perceptual metric. In *Proc. IEEE Conference on Computer Vision and Pattern Recognition (CVPR)*, pp. 586–595, 2018.

A Derivations

A.1 SQ-VAE-2

The ELBO of SQ-VAE-2 is formulated by using Bayes' theorem as

$$\begin{aligned}
\log p_{\boldsymbol{\theta}}(\boldsymbol{x}) &\geq \log p_{\boldsymbol{\theta}}(\boldsymbol{x}) - D_{\mathrm{KL}}(\mathcal{Q}(\boldsymbol{Z}_{1:L}, \tilde{\boldsymbol{Z}}_{1:L}|\boldsymbol{x}) \parallel \mathcal{P}(\boldsymbol{Z}_{1:L}, \tilde{\boldsymbol{Z}}_{1:L}|\boldsymbol{x})) \\
&= \mathbb{E}_{\mathcal{Q}(\boldsymbol{Z}_{1:L}, \tilde{\boldsymbol{Z}}_{1:L}|\boldsymbol{x})}\left[\log \frac{p_{\boldsymbol{\theta}}(\boldsymbol{x})\mathcal{P}(\boldsymbol{Z}_{1:L}, \tilde{\boldsymbol{Z}}_{1:L}|\boldsymbol{x})}{\mathcal{Q}(\boldsymbol{Z}_{1:L}, \tilde{\boldsymbol{Z}}_{1:L}|\boldsymbol{x})}\right] \\
&= \mathbb{E}_{\mathcal{Q}(\boldsymbol{Z}_{1:L}, \tilde{\boldsymbol{Z}}_{1:L}|\boldsymbol{x})}\left[\log p_{\boldsymbol{\theta}}(\boldsymbol{x}|\boldsymbol{Z}_{1:L}) - \log \frac{\mathcal{Q}(\boldsymbol{Z}_{1:L}, \tilde{\boldsymbol{Z}}_{1:L}|\boldsymbol{x})}{\mathcal{P}(\boldsymbol{Z}_{1:L}, \tilde{\boldsymbol{Z}}_{1:L})}\right] \\
&= \mathbb{E}_{\mathcal{Q}(\boldsymbol{Z}_{1:L}, \tilde{\boldsymbol{Z}}_{1:L}|\boldsymbol{x})}\left[\log p_{\boldsymbol{\theta}}(\boldsymbol{x}|\boldsymbol{Z}_{1:L}) - \sum_{l=1}^{L}\sum_{i=1}^{d_l}\left(\log \frac{p_{s_l^2}(\tilde{\boldsymbol{z}}_{l,i}|\hat{\boldsymbol{Z}}_l)}{p_{s_l^2}(\tilde{\boldsymbol{z}}_{l,i}|\boldsymbol{Z}_l)} + \log \frac{\hat{P}_{s_l^2}(\boldsymbol{z}_{l,i}|\tilde{\boldsymbol{Z}}_l)}{P(\boldsymbol{z}_{l,i})}\right)\right] \\
&= \mathbb{E}_{\mathcal{Q}(\boldsymbol{Z}_{1:L}, \tilde{\boldsymbol{Z}}_{1:L}|\boldsymbol{x})}\left[\log p_{\boldsymbol{\theta}}(\boldsymbol{x}|\boldsymbol{Z}_{1:L}) + \sum_{l=1}^{L}\sum_{i=1}^{d_l}\left(\log \frac{p_{s_l^2}(\tilde{\boldsymbol{z}}_{l,i}|\boldsymbol{Z}_l)}{p_{s_l^2}(\tilde{\boldsymbol{z}}_{l,i}|\hat{\boldsymbol{Z}}_l)} + H(\hat{P}_{s_l^2}(\boldsymbol{z}_{l,i}|\tilde{\boldsymbol{Z}}_l)) - \log K_l\right)\right]. \qquad (17)
\end{aligned}$$

Since the probabilistic parts are modeled as Gaussian distributions, the first and second terms can be calculated as

$$\begin{aligned}
\log p_{\boldsymbol{\theta}}(\boldsymbol{x}|\boldsymbol{Z}_{1:L}) &= \log \mathcal{N}(\boldsymbol{x}; \boldsymbol{f}_{\boldsymbol{\theta}}(\boldsymbol{Z}_{1:L}), \sigma^2\boldsymbol{I}) \\
&= -\frac{D}{2}\log(2\pi\sigma^2) - \frac{1}{2\sigma^2}\|\boldsymbol{x} - \boldsymbol{f}_{\boldsymbol{\theta}}(\boldsymbol{x})\|_2^2 \quad \text{and} \qquad (18)
\end{aligned}$$

$$\begin{aligned}
\mathbb{E}_{\mathcal{Q}(\boldsymbol{Z}_{1:L}, \tilde{\boldsymbol{Z}}_{1:L}|\boldsymbol{x})}\left[\frac{p_{s_l^2}(\tilde{\boldsymbol{z}}_{l,i}|\boldsymbol{Z}_l)}{p_{s_l^2}(\tilde{\boldsymbol{z}}_{l,i}|\hat{\boldsymbol{Z}}_l)}\right] &= \mathbb{E}_{\mathcal{Q}(\boldsymbol{Z}_{1:L}, \tilde{\boldsymbol{Z}}_{1:L}|\boldsymbol{x})}\left[-\frac{1}{2s_l^2}\|\tilde{\boldsymbol{z}}_{l,i} - \boldsymbol{z}_{l,i}\|_2^2 + \frac{1}{2s_l^2}\|\tilde{\boldsymbol{z}}_{l,i} - \hat{\boldsymbol{z}}_{l,i}\|_2^2\right] \\
&= -\mathbb{E}_{\mathcal{Q}(\boldsymbol{Z}_{1:L}, \tilde{\boldsymbol{Z}}_{1:L}|\boldsymbol{x})}\left[\frac{1}{2s_l^2}\|\tilde{\boldsymbol{z}}_{l,i} - \boldsymbol{z}_{l,i}\|_2^2\right] + \frac{d_b}{2}. \qquad (19)
\end{aligned}$$

By substituting Equations (18) and (19) into Equation (17), we have Equation (7), where we use $\tilde{\boldsymbol{Z}}_l = \hat{\boldsymbol{Z}}_l$ instead of sampling it in practical implementation.

A.2 RSQ-VAE

The ELBO of RSQ-VAE is formulated by using Bayes' theorem as

$$\begin{aligned}
\log p_{\boldsymbol{\theta}}(\boldsymbol{x}) &\geq \log p_{\boldsymbol{\theta}}(\boldsymbol{x}) - D_{\mathrm{KL}}(\mathcal{Q}(\boldsymbol{Z}_{1:L}, \tilde{\boldsymbol{Z}}|\boldsymbol{x}) \parallel \mathcal{P}(\boldsymbol{Z}_{1:L}, \tilde{\boldsymbol{Z}}|\boldsymbol{x})) \\
&= \mathbb{E}_{\mathcal{Q}(\boldsymbol{Z}_{1:L}, \tilde{\boldsymbol{Z}}_{1:L}|\boldsymbol{x})}\left[\log \frac{p_{\boldsymbol{\theta}}(\boldsymbol{x})\mathcal{P}(\boldsymbol{Z}_{1:L}, \tilde{\boldsymbol{Z}}|\boldsymbol{x})}{\mathcal{Q}(\boldsymbol{Z}_{1:L}, \tilde{\boldsymbol{Z}}|\boldsymbol{x})}\right] \\
&= \mathbb{E}_{\mathcal{Q}(\boldsymbol{Z}_{1:L}, \tilde{\boldsymbol{Z}}|\boldsymbol{x})}\left[\log p_{\boldsymbol{\theta}}(\boldsymbol{x}|\boldsymbol{Z}_{1:L}) - \log \frac{\mathcal{Q}(\boldsymbol{Z}_{1:L}, \tilde{\boldsymbol{Z}}|\boldsymbol{x})}{\mathcal{P}(\boldsymbol{Z}_{1:L}, \tilde{\boldsymbol{Z}})}\right] \\
&= \mathbb{E}_{\mathcal{Q}(\boldsymbol{Z}_{1:L}, \tilde{\boldsymbol{Z}}|\boldsymbol{x})}\left[\log p_{\boldsymbol{\theta}}(\boldsymbol{x}|\boldsymbol{Z}_{1:L}) - \sum_{i=1}^{d_l}\log \frac{p_{\boldsymbol{s}^2}(\tilde{\boldsymbol{z}}_i|\hat{\boldsymbol{Z}})}{p_{\boldsymbol{s}^2}(\tilde{\boldsymbol{z}}_i|\boldsymbol{Z})} - \sum_{l=1}^{L}\sum_{i=1}^{d_l}\log \frac{\hat{P}_{s_l^2}(\boldsymbol{z}_{l,i}|\tilde{\boldsymbol{Z}}_l)}{P(\boldsymbol{z}_{l,i})}\right] \\
&= \mathbb{E}_{\mathcal{Q}(\boldsymbol{Z}_{1:L}, \tilde{\boldsymbol{Z}}|\boldsymbol{x})}\left[\log p_{\boldsymbol{\theta}}(\boldsymbol{x}|\boldsymbol{Z}_{1:L}) + \sum_{i=1}^{d_l}\log \frac{p_{\boldsymbol{s}^2}(\tilde{\boldsymbol{z}}_i|\boldsymbol{Z})}{p_{\boldsymbol{s}^2}(\tilde{\boldsymbol{z}}_i|\hat{\boldsymbol{Z}})} + \sum_{l=1}^{L}\sum_{i=1}^{d_l} H(\hat{P}_{s_l^2}(\boldsymbol{z}_{l,i}|\tilde{\boldsymbol{Z}}_l)) - \log K_l\right]. \qquad (20)
\end{aligned}$$

Since the probabilistic parts are modeled as Gaussian distributions, the second term can be calculated as

$$\begin{aligned}
\mathbb{E}_{\mathcal{Q}(\boldsymbol{Z}_{1:L}, \tilde{\boldsymbol{Z}}|\boldsymbol{x})}\left[\frac{p_{\boldsymbol{s}^2}(\tilde{\boldsymbol{z}}_i|\boldsymbol{Z})}{p_{\boldsymbol{s}^2}(\tilde{\boldsymbol{z}}_i|\hat{\boldsymbol{Z}})}\right] &= \mathbb{E}_{\mathcal{Q}(\boldsymbol{Z}_{1:L}, \tilde{\boldsymbol{Z}}|\boldsymbol{x})}\left[-\frac{1}{2\sum_{l=1}^{L} s_l^2}\|\tilde{\boldsymbol{z}}_i - \boldsymbol{z}_i\|_2^2 + \frac{1}{2\sum_{l=1}^{L} s_l^2}\|\tilde{\boldsymbol{z}}_i - \hat{\boldsymbol{z}}_i\|_2^2\right] \\
&= -\mathbb{E}_{\mathcal{Q}(\boldsymbol{Z}_{1:L}, \tilde{\boldsymbol{Z}}|\boldsymbol{x})}\left[\frac{1}{2\sum_{l=1}^{L} s_l^2}\|\tilde{\boldsymbol{z}}_i - \boldsymbol{z}_i\|_2^2\right] + \frac{d_b}{2}. \qquad (21)
\end{aligned}$$

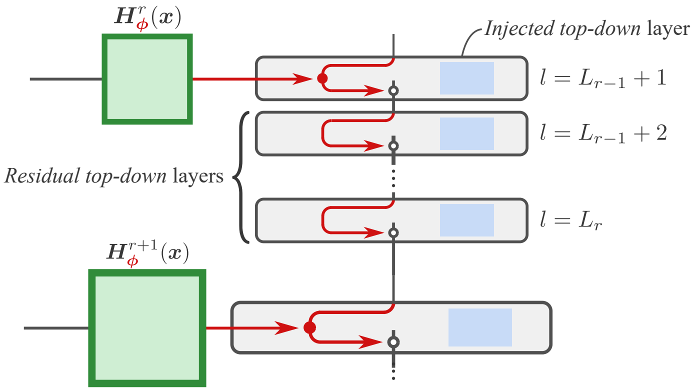
$\boldsymbol{H}^r_{\boldsymbol{\phi}}(\boldsymbol{x})$
Injected top-down layer
$l = L_{r-1}+1$
$l = L_{r-1}+2$
Residual top-down layers
$l = L_r$
$\boldsymbol{H}^{r+1}_{\boldsymbol{\phi}}(\boldsymbol{x})$

Figure 5: *Top-down* layers corresponding to the rth resolution in hybrid model in Appendix B.

By substituting Equations (18) and (21) into (20), we have Equation (15), where we use $\tilde{\boldsymbol{Z}} = \boldsymbol{H}_{\boldsymbol{\phi}}(\boldsymbol{x})$ instead of sampling it in practical implementation. We have derived the ELBO objective in the case of $R = 1$. We extend the model to the general case of R, equivalent to the hybrid model, in Appendix B.

B Hybrid model

We provide the ELBO of a hybrid model, where the two types of *top-down* layers are combinatorially used to build a *top-down* path as in Figure 5. We introduce some extra notations: L_r indicates the number of layers corresponding to the resolutions from the first to rth order; $\ell_r := \{L_{r-1}+1, \cdots, L_r\}$ is a set of all the layers corresponding to the resolution r; and the output of the encoding block in the $(L_{r-1}+1)$th layer is denoted as $\tilde{\boldsymbol{G}}^r_{\boldsymbol{\phi}}(\boldsymbol{H}^r_{\boldsymbol{\phi}}(\boldsymbol{x}), \boldsymbol{Z}_{1:L_{r-1}})$. In Figure 5, the quantized variables $\boldsymbol{Z}_{\ell_r}$ aim at approximating the variable encoded at $l = L_{r-1}+1$ as

$$\tilde{\boldsymbol{G}}^r_{\boldsymbol{\phi}}(\boldsymbol{H}^r_{\boldsymbol{\phi}}(\boldsymbol{x}), \boldsymbol{Z}_{1:L_{r-1}}) \approx \sum_{l\in\ell_r} \boldsymbol{Z}_l =: \boldsymbol{Y}_r. \tag{22}$$

On this basis, the lth *top-down* layer quantizes the following information:

$$\hat{\boldsymbol{Z}}_l = \boldsymbol{G}^l_{\boldsymbol{\phi}}(\boldsymbol{x}, \boldsymbol{Z}_{1:l-1}) = \begin{cases} \boldsymbol{H}^1_{\boldsymbol{\phi}}(\boldsymbol{x}) & (l=1) \\ \tilde{\boldsymbol{G}}^{r(l)}_{\boldsymbol{\phi}}(\boldsymbol{H}^{r(l)}_{\boldsymbol{\phi}}(\boldsymbol{x}), \boldsymbol{Z}_{1:L_{r(l)-1}}) - \sum_{l'=L_{r(l)-1}+1}^{l} \boldsymbol{Z}_{l'} & (l>1). \end{cases} \tag{23}$$

To derive the ELBO objective, we consider conditional distributions on $(\boldsymbol{Z}_{1:L}, \tilde{\boldsymbol{Y}}_{1:R})$, where $\tilde{\boldsymbol{Y}}_r := \sum_{l\in\ell_r} \tilde{\boldsymbol{Z}}_l$. From the reproductive property of Gaussian distribution, the continuous latent variable converted from $\boldsymbol{Y}_r$ via the stochastic dequantization processes, $\tilde{\boldsymbol{Z}}_{\ell_r}$, follows the following Gaussian distribution:

$$p_{\boldsymbol{s}^2_r}(\tilde{\boldsymbol{y}}_{r,i}|\boldsymbol{Z}_{\ell_r}) = \mathcal{N}\left(\tilde{\boldsymbol{y}}_{r,i}; \sum_{l\in\ell_r} \boldsymbol{z}_{l,i}, \left(\sum_{l\in\ell_r} s^2_l\right)\boldsymbol{I}\right), \tag{24}$$

where $\boldsymbol{s}^2_r := \{s^2_l\}_{l\in\ell_r}$. We use the following prior distribution to derive the ELBO objective:

$$\mathcal{P}(\boldsymbol{Z}_{1:L}, \tilde{\boldsymbol{Y}}_{1:R}) = \prod_{r=1}^{R}\prod_{i=1}^{d_r}\left(\prod_{l\in\ell_r} P(\boldsymbol{z}_{l,i})\right) p_{\boldsymbol{s}^2_r}(\tilde{\boldsymbol{y}}_{r,i}|\boldsymbol{Z}_{\ell_r}), \tag{25}$$

where $d_r := d_l$ for $l \in \ell_r$. With the prior and posterior distributions, the ELBO of the hybrid model is formulated by using Bayes' theorem as

$$\begin{aligned}
\log p_{\boldsymbol{\theta}}(\boldsymbol{x}) &\geq \log p_{\boldsymbol{\theta}}(\boldsymbol{x}) - D_{\mathrm{KL}}(\mathcal{Q}(\boldsymbol{Z}_{1:L}, \tilde{\boldsymbol{Y}}_{1:R}|\boldsymbol{x}) \parallel \mathcal{P}(\boldsymbol{Z}_{1:L}, \tilde{\boldsymbol{Y}}_{1:R}|\boldsymbol{x})) \\
&= \mathbb{E}_{\mathcal{Q}(\boldsymbol{Z}_{1:L}, \tilde{\boldsymbol{Y}}_{1:R}|\boldsymbol{x})}\left[\log \frac{p_{\boldsymbol{\theta}}(\boldsymbol{x})\mathcal{P}(\boldsymbol{Z}_{1:L}, \tilde{\boldsymbol{Y}}_{1:R}|\boldsymbol{x})}{\mathcal{Q}(\boldsymbol{Z}_{1:L}, \tilde{\boldsymbol{Y}}_{1:R}|\boldsymbol{x})}\right] \\
&= \mathbb{E}_{\mathcal{Q}(\boldsymbol{Z}_{1:L}, \tilde{\boldsymbol{Y}}_{1:R}|\boldsymbol{x})}\left[\log p_{\boldsymbol{\theta}}(\boldsymbol{x}|\boldsymbol{Z}_{1:L}) - \log \frac{\mathcal{Q}(\boldsymbol{Z}_{1:L}, \tilde{\boldsymbol{Y}}_{1:R}|\boldsymbol{x})}{\mathcal{P}(\boldsymbol{Z}_{1:L}, \tilde{\boldsymbol{Y}}_{1:R})}\right] \\
&= \mathbb{E}_{\mathcal{Q}(\boldsymbol{Z}_{1:L}, \tilde{\boldsymbol{Y}}_{1:R}|\boldsymbol{x})}\left[\log p_{\boldsymbol{\theta}}(\boldsymbol{x}|\boldsymbol{Z}_{1:L}) - \sum_{r=1}^{R}\sum_{i=1}^{d_r} \log \frac{p_{\boldsymbol{s}_r^2}(\tilde{\boldsymbol{y}}_{r,i}|\hat{\boldsymbol{Z}}_{\ell_r})}{p_{\boldsymbol{s}_r^2}(\tilde{\boldsymbol{y}}_{r,i}|\boldsymbol{Z}_{\ell_r})} - \sum_{l=1}^{L}\sum_{i=1}^{d_l} \log \frac{\hat{P}_{s_l^2}(\boldsymbol{z}_{l,i}|\tilde{\boldsymbol{Z}}_l)}{P(\boldsymbol{z}_{l,i})}\right] \\
&= \mathbb{E}_{\mathcal{Q}(\boldsymbol{Z}_{1:L}, \tilde{\boldsymbol{Y}}_{1:R}|\boldsymbol{x})}\left[\log p_{\boldsymbol{\theta}}(\boldsymbol{x}|\boldsymbol{Z}_{1:L}) + \sum_{r=1}^{R}\sum_{i=1}^{d_r} \log \frac{p_{\boldsymbol{s}_r^2}(\tilde{\boldsymbol{y}}_{r,i}|\boldsymbol{Z}_{\ell_r})}{p_{\boldsymbol{s}_r^2}(\tilde{\boldsymbol{y}}_{r,i}|\hat{\boldsymbol{Z}}_{\ell_r})} + \sum_{l=1}^{L}\sum_{i=1}^{d_l} H(\hat{P}_{s_l^2}(\boldsymbol{z}_{l,i}|\tilde{\boldsymbol{Z}}_l)) - \log K_l\right],
\end{aligned} \tag{26}$$

where $\hat{\boldsymbol{Y}}_r = \tilde{\boldsymbol{G}}_{\boldsymbol{\phi}}^r(\boldsymbol{H}_{\boldsymbol{\phi}}^r(\boldsymbol{x}), \boldsymbol{Z}_{1:L_{r-1}})$. Since we model the dequantization process and the probabilistic decoder as Gaussians, by substituting their closed forms into the above equation, we have

$$\begin{aligned}
\mathcal{J}_{\text{HQ-VAE}} &= \frac{D}{2}\log\sigma^2 \\
&+ \mathbb{E}_{\mathcal{Q}(\boldsymbol{Z}_{1:L}, \tilde{\boldsymbol{Z}}_{1:L}|\boldsymbol{x})}\left[\frac{\|\boldsymbol{x} - \boldsymbol{f}_{\boldsymbol{\theta}}(\boldsymbol{Z}_{1:L})\|_2^2}{2\sigma^2} + \sum_{r=1}^{R} \frac{\left\|\tilde{\boldsymbol{G}}_{\boldsymbol{\phi}}^r(\boldsymbol{H}_{\boldsymbol{\phi}}^r(\boldsymbol{x}), \boldsymbol{Z}_{1:L_{r-1}}) - \sum_{l\in\ell_r}\boldsymbol{Z}_l\right\|_F^2}{2\sum_{l\in\ell_r} s_l^2} - \sum_{l=1}^{L} H(\hat{P}_{s_l^2}(\boldsymbol{Z}_l|\tilde{\boldsymbol{Z}}_l))\right],
\end{aligned} \tag{27}$$

where we used

$$\begin{aligned}
\mathbb{E}_{\mathcal{Q}(\boldsymbol{Z}_{1:L}, \tilde{\boldsymbol{Y}}_{1:R}|\boldsymbol{x})}\left[\frac{p_{\boldsymbol{s}_r^2}(\tilde{\boldsymbol{y}}_{r,i}|\boldsymbol{Z}_{\ell_r})}{p_{\boldsymbol{s}_r^2}(\tilde{\boldsymbol{y}}_{r,i}|\hat{\boldsymbol{Z}}_{\ell_r})}\right] &= \mathbb{E}_{\mathcal{Q}(\boldsymbol{Z}_{1:L}, \tilde{\boldsymbol{Y}}_{1:R}|\boldsymbol{x})}\left[-\frac{1}{2\sum_{l\in\ell_r} s_l^2}\|\tilde{\boldsymbol{y}}_{r,i} - \boldsymbol{y}_{r,i}\|_2^2 + \frac{1}{2\sum_{l\in\ell_r} s_l^2}\|\tilde{\boldsymbol{y}}_{r,i} - \hat{\boldsymbol{y}}_{r,i}\|_2^2\right] \\
&= -\mathbb{E}_{\mathcal{Q}(\boldsymbol{Z}_{1:L}, \tilde{\boldsymbol{Y}}_{1:R}|\boldsymbol{x})}\left[\frac{1}{2\sum_{l\in\ell_r} s_l^2}\|\tilde{\boldsymbol{y}}_{r,i} - \boldsymbol{y}_{r,i}\|_2^2\right] + \frac{d_r}{2}.
\end{aligned} \tag{28}$$

Here, we use $\tilde{\boldsymbol{Y}}_r = \hat{\boldsymbol{Y}}_r$ instead of sampling it in practical implementation.

C Experimental details

We explain the details of the experiments[2] in Section 5. For all the experiments except for RSQ-VAE and RQ-VAE on FFHQ and UrbanSound8K in Section 5.2, we construct architectures for both the *bottom-up* and *top-down* paths as described in Figures 1 and 6. To build these paths, we introduce two common blocks, the Resblock and Convblock by following Child (2021) as in Figure 6a, which are used in Figures 6b and 6c. Here, we denote the width and height of $\boldsymbol{H}_{\boldsymbol{\phi}}^r(\boldsymbol{x})$ as w_r and h_r, respectively, i.e., $\boldsymbol{H}_{\boldsymbol{\phi}}^r(\boldsymbol{x}) \in \mathbb{R}^{d_b \times w_r \times h_r}$. We set $c_{\text{mid}} = 0.5$ in Figure 6. For all the experiments, we use the Adam optimizer with $\beta_1 = 0.9$ and $\beta_2 = 0.9$. Unless otherwise noted, we reduce the learning rate in half if the validation loss is not improved in the last three epochs.

In HQ-VAE, we deal with the decoder variance σ^2 using the update scheme with the maximum likelihood estimation Takida et al. (2022a). We gradually reduce the temperature parameter of Gumbel–softmax trick with a standard scheduler $\tau = \exp(10^{-5} \cdot t)$ Jang et al. (2017), where t is the iteration step.

We set hyperparameters of VQ-VAE to standard parameter values: the balancing parameter β in Equations (8) and (16) to 0.25, and the weight decay in EMA for the codebook update to 0.99, respectively.

---

[2] The source code is attached in the supplementary material.

Table 3: Notations of convolutional layers used in Figure 6.

Notation	Description
$\text{Conv}_d^{(1\times1)}$	2D Convolutional layer (channel= n, kernel= 1×1, stride= 1, padding= 0)
$\text{Conv}_d^{(3\times3)}$	2D Convolutional layer (channel= n, kernel= 3×3, stride= 1, padding= 1)
$\text{Conv}_d^{(4\times4)}$	2D Convolutional layer (channel= n, kernel= 4×4, stride= 2, padding= 1)
$\text{ConvT}_d^{(3\times3)}$	2D Transpose convolutional layer (channel= n, kernel= 3×3, stride= 1, padding= 1)
$\text{ConvT}_d^{(4\times4)}$	2D Transpose convolutional layer (channel= n, kernel= 4×4, stride= 2, padding= 1)

We here review the datasets used in Section 5 below.

CIFAR10. CIFAR10 Krizhevsky et al. (2009) contains 10 classes of 32×32 color images, which are separated into 50,000 and 10,000 samples for train and test sets, respectively. We use the default split and further randomly select 10,000 samples from the train set to prepare the validation set.

CelebA-HQ. CelebA-HQ Karras et al. (2018) contains 30,000 high-resolution face images that are selected from the CelebA dataset by following Karras et al. (2018). We use the default train/validation/test split. We preprocess the images by cropping and resizing them to the size of 256×256.

FFHQ. FFHQ Karras et al. (2019) contains 70,000 high-resolution face images. In Section 5.1, we split the images into three sets: train (60,000 samples), validation (5,000 samples), and test (5,000 samples) sets. We crop and resize them to 1024×1024. In Section 5.2, we follow the same preprocessing as in Lee et al. (2022a), respectively, where it splits the images into two sets, train (60,000 samples), validation (10,000 samples) sets and crop and resize them to 256×256.

ImageNet. ImageNet Deng et al. (2009) contains 1000 classes of natural images in RGB scales. We use the default train/val/test split. We crop and resize the images to 256×256.

UrbanSound8K. UrbanSound8K Salamon et al. (2014) contains 8,732 labeled audio clips of urban sound from 10 classes. UrbanSound8K has a wide range of sound classes, such as dog barking and drilling. UrbanSound8K is divided into 10 folds, and we use the fold 1-8/9/10 as the train/validation/test split. The duration of each audio clip is less than 4 seconds. In our experiments, to align the length of input audio, we pad the all audio clips to 4 seconds. We also convert the all audio clips to 16 bit and down-sampled them to 22,050 kHz. A 4-second waveform audio clip is converted to a Mel spectrogram with shape 80×344. We preprocess an audio clip following the paper Liu et al. (2021):

1. We extract an 80-dimensional Mel spectrogram using the short-time Fourier transform (STFT) with a frame size of 1024, a hop size of 256, and a Hann window.
2. We apply dynamic range compression to the Mel spectrogram by first clipping it to a minimum value of 1×10^{-5} and then applying a logarithmic transformation.

C.1 SQ-VAE-2 vs VQ-VAE-2

C.1.1 Comparison on CIFAR10 and CelebA-HQ

We construct the architecture as depicted in Figures 1 and 6. To build the *top-down* paths, we use two *injected top-down* layers (i.e., $R = 2$) with $w_1 = h_1 = 8$ and $w_2 = h_2 = 16$ for CIFAR10, and three layers (i.e., $R = 3$) with $w_1 = h_1 = 8$, $w_2 = h_2 = 16$ and $w_3 = h_3 = 32$ for CelebA-HQ, respectively. For the *bottom-up* paths, we repeatedly stack two Resblocks and an average pooling layer once and four times, respectively, for CIFAR10 and CelebA-HQ. We set the learning rate to 0.001 and train all the models for a maximum of 100 epochs with a mini-batch size of 32.

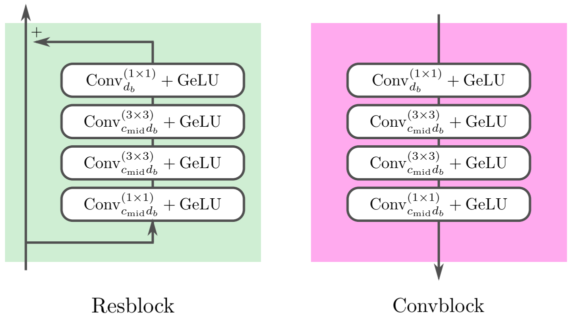
+
$\mathrm{Conv}_{d_b}^{(1\times1)}$ + GeLU
$\mathrm{Conv}_{c_{\mathrm{mid}}d_b}^{(3\times3)}$ + GeLU
$\mathrm{Conv}_{c_{\mathrm{mid}}d_b}^{(3\times3)}$ + GeLU
$\mathrm{Conv}_{c_{\mathrm{mid}}d_b}^{(1\times1)}$ + GeLU
$\mathrm{Conv}_{d_b}^{(1\times1)}$ + GeLU
$\mathrm{Conv}_{c_{\mathrm{mid}}d_b}^{(3\times3)}$ + GeLU
$\mathrm{Conv}_{c_{\mathrm{mid}}d_b}^{(3\times3)}$ + GeLU
$\mathrm{Conv}_{c_{\mathrm{mid}}d_b}^{(1\times1)}$ + GeLU
Resblock
Convblock

(a) Basic blocks.

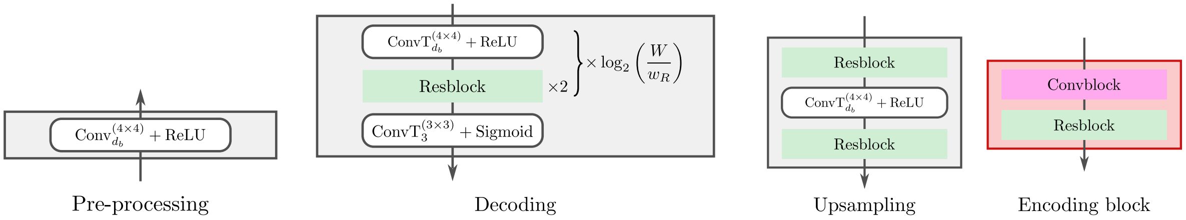
$\mathrm{Conv}_{d_b}^{(4\times4)}$ + ReLU
Pre-processing
$\mathrm{ConvT}_{d_b}^{(4\times4)}$ + ReLU
Resblock
×2
$\times\log_2\left(\frac{W}{w_R}\right)$
$\mathrm{ConvT}_{3}^{(3\times3)}$ + Sigmoid
Decoding
Resblock
$\mathrm{ConvT}_{d_b}^{(4\times4)}$ + ReLU
Resblock
Upsampling
Convblock
Resblock
Encoding block

(b) Pre-processing and decoding

(c) Blocks in *top-down* layer

Figure 6: Architecture details in Figure 1. Notations of convolutional layers, $\mathrm{Conv}_d^{(k\times k)}$ and $\mathrm{ConvT}_d^{(k\times k)}$, are summarized in Table 3.

C.1.2 Comparison on large-scale datasets

We construct the architecture as depicted in Figures 1 and 6. To build the *top-down* paths, we use two *injected top-down* layers (i.e., $R = 2$), with $w_1 = h_1 = 32$ and $w_2 = h_2 = 64$ for ImageNet, and three layers (i.e., $R = 3$) with $w_1 = h_1 = 32$, $w_2 = h_2 = 64$ and $w_3 = h_3 = 128$ for FFHQ, respectively. For the *bottom-up* paths, we repeatedly stack two Resblocks and an average pooling layer three times and five times respectively for ImageNet and FFHQ. We set the learning rate to 0.0005. We train ImageNet and FFHQ for a maximum of 50 and 200 epochs with a mini-batch size of 512 and 128, respectively. Figure 7 and Figure 8 show reconstructed samples of SQ-VAE-2 on ImageNet and FFHQ, respectively.

C.2 RSQ-VAE vs RQ-VAE

C.2.1 Comparison on CIFAR10 and CelebA-HQ

We construct the architecture as depicted in Figures 1 and 6 without *injected top-down* layers, i.e., $R = 1$. We set the resolution of $\boldsymbol{H}_{\boldsymbol{\phi}}(\boldsymbol{x})$ to $w = h = 8$. For the *bottom-up* paths, we repeatedly stack two Resblocks and an average pooling layer once and four times, respectively, for CIFAR10 and CelebA-HQ. We set the learning rate to 0.001 and train all the models for a maximum of 100 epochs with a mini-batch size of 32.

C.2.2 Improvement in perceptual quality

In this experiment, we use the same network architecture as that used in Lee et al. (2022a). We set the learning rate to 0.001 and train an RSQ-VAE model for a maximum of 300 epochs with a mini-batch size of 128 (4 GPUs, 32 samples for each GPU) on FFHQ. We use our modified LPIPS loss (see Appendix C.4) in training. For evaluation, we compute rFID scores with the code provided in their repository[3] on the validation set (10,000 samples). And, we use the pre-trained RQ-VAE model offered in the same repository for evaluating RQ-VAE.

We show examples of reconstructed images in Appendix C.4 after we explain our modified LPIPS loss.

---

[3] `https://github.com/kakaobrain/rq-vae-transformer`

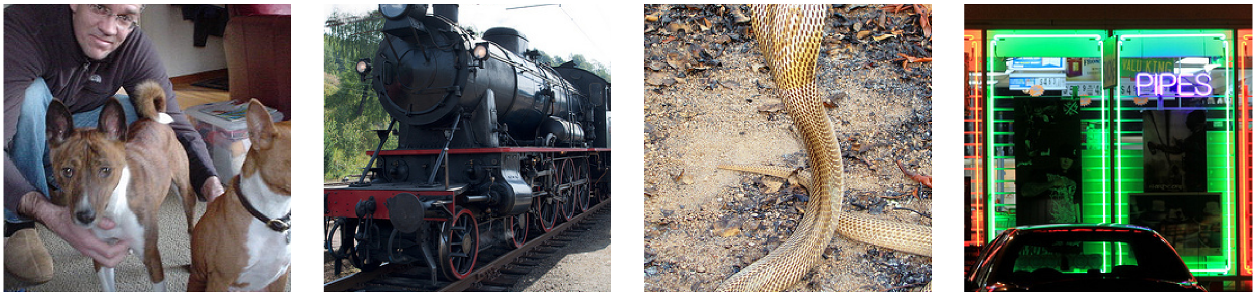

(a) Source images

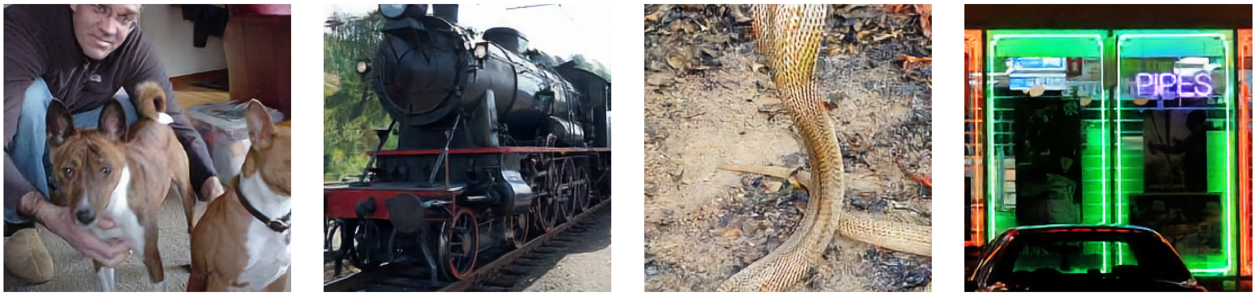

(b) Reconstructed images

Figure 7: Reconstructed samples of SQ-VAE-2 trained on ImageNet

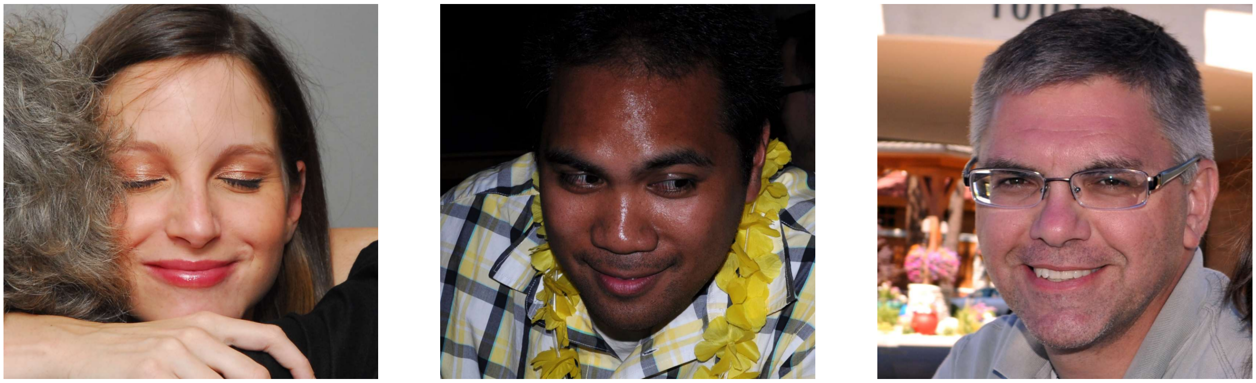

(a) Source images

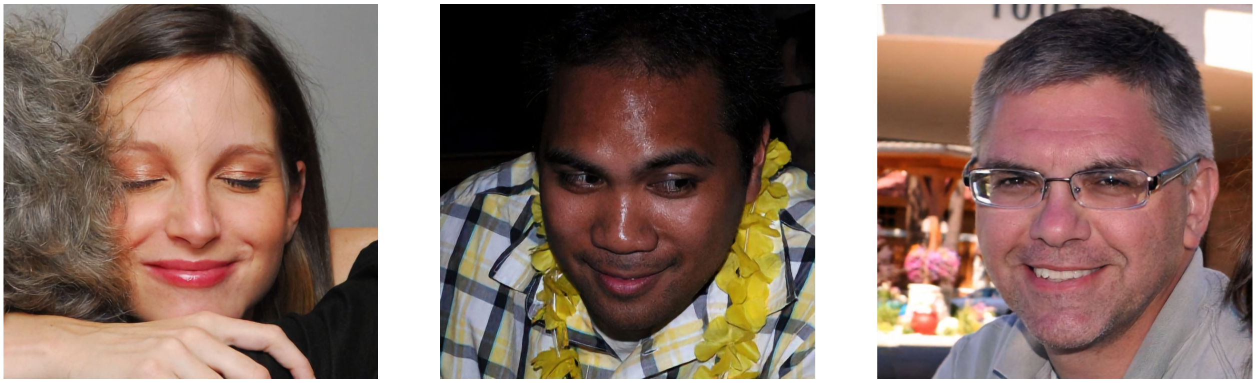

(b) Reconstructed images

Figure 8: Reconstructed samples of SQ-VAE-2 trained on FFHQ

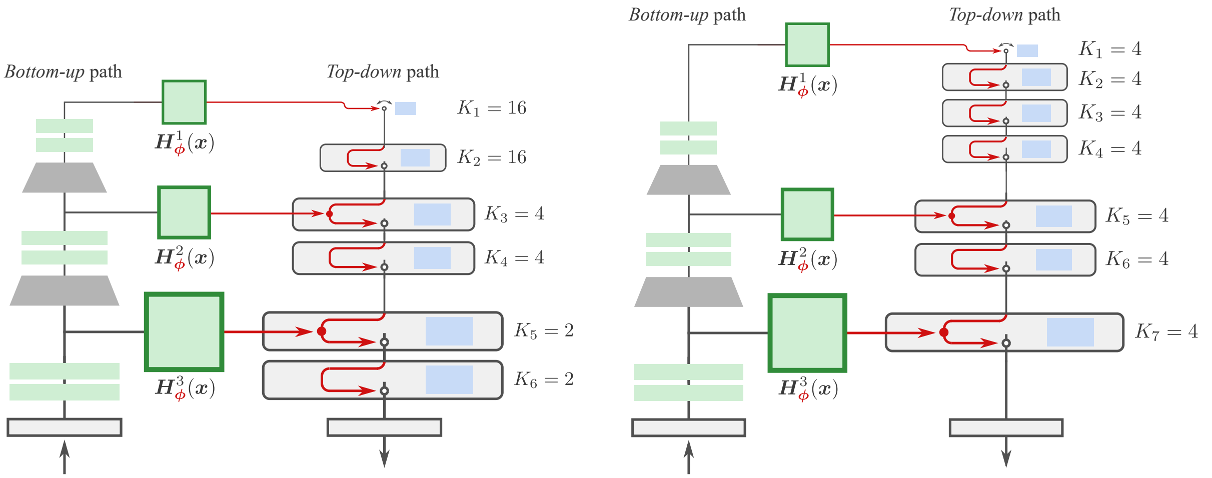

(a) Case1: $\ell_1 = \{1, 2\}$, $\ell_2 = \{3, 4\}$ and $\ell_3 = \{5, 6\}$ (b) Case2: $\ell_1 = \{1, 2, 3, 4\}$, $\ell_2 = \{5, 6\}$ and $\ell_3 = \{7\}$

Figure 9: Architecture of the hybrid model in Appendix C.3.

C.2.3 Validation on an audio dataset

We construct the architecture by following the previous audio generation work Liu et al. (2021). For the *top-down* paths, the architecture consists of several strided convolutional layers in parallel Xian et al. (2021). We use four strided convolutional layers consisting of two sub-layers with stride 2, followed by two ResBlocks with ReLU activations. The kernel sizes of these four strided convolutional layers are 2×2, 4×4, 6×6 and 8×8 respectively. We add the outputs of the four strided convolutional layers, and pass it to a convolutional layer with kernel size 3×3. Then we get the resolution of $\boldsymbol{H}_{\boldsymbol{\phi}}(\boldsymbol{x})$ to $w = 20, h = 86$. For the *bottom-up* paths, we stack a convolutional layer with kernel size 3×3, two Resblocks with ReLU activations, and two transposed convolutional layers with stride 2 and kernel size 4×4. We set the learning rate to 0.001 and train all the models for a maximum of 100 epochs with a mini-batch size of 32.

As an example of demonstration, we randomly select audio clips from our test split of UrbanSound8K and show their reconstructed Mel spectrogram samples from RQ-VAE and RSQ-VAE in Figure 10. While the samples from RQ-VAE have difficulty to reconstruct the sources with shared codebooks, the samples from RSQ-VAE reconstruct detailed features of the sources.

C.3 Empirical study of top-down layers

For a demonstration, we build two HQ-VAEs by combinatorially using both the *injected top-down* and the *residual top-down* layers with three resolutions, $w_1 = h_1 = 16$, $w_2 = h_2 = 32$ and $w_3 = h_3 = 64$. We construct the architectures as described in Figure 9 and train them on CelebA-HQ. Figure 12 shows the progressively reconstructed images for each case. We can observe the same tendencies as in Figures 4a and 4c.

C.4 Perceptual loss for images

We found that LPIPS loss Zhang et al. (2018), which is a perceptual loss for images Johnson et al. (2016), works well with our HQ-VAE. However, we also noticed that just replacing $\|\boldsymbol{x} - \boldsymbol{f}_{\boldsymbol{\theta}}(\boldsymbol{Z}_{1:L})\|_2^2$ in the objective function of HQ-VAE (Equations (7) and (15)) with an LPIPS loss $\mathcal{L}_{\text{LPIPS}}(\boldsymbol{x}, \boldsymbol{f}_{\boldsymbol{\theta}}(\boldsymbol{Z}_{1:L}))$ leads to artifacts in generated images. We hypothesize that those artifacts are caused by the max-pooling layers in VGGNet used in LPIPS. Signals from VGGNet might not reach all pixels in backpropagation due to the max-pooling layers. To mitigate this issue, we applied a padding-and-trimming operation to both a generated image $\boldsymbol{f}_{\boldsymbol{\theta}}(\boldsymbol{Z}_{1:L})$ and the corresponding reference image $\boldsymbol{x}$ before the LPIPS loss function. That is $\mathcal{L}_{\text{LPIPS}}(\text{pt}\,[\boldsymbol{x}]\,, \text{pt}\,[\boldsymbol{f}_{\boldsymbol{\theta}}(\boldsymbol{Z}_{1:L})])$, where pt [ ] denotes our padding-and-trimming operator. The PyTorch implementation of such an operation is described below.

```
import random
import torch
import torch.nn.functional as F

def padding_and_trimming(
    x_rec, # decoder output
    x  # reference image
):
    _, _, H, W = x.size()

    x_rec = F.pad(x_rec, (15, 15, 15, 15), mode='replicate')
    x = F.pad(x, (15, 15, 15, 15), mode='replicate')

    _, _, H_pad, W_pad = x.size()
    top = random.randrange(0, 16)
    bottom = H_pad - random.randrange(0, 16)
    left = random.randrange(0, 16)
    right = W_pad - random.randrange(0, 16)

    x_rec = F.interpolate(x_rec[:, :, top:bottom, left:right],
                          size=(H, W), mode='bicubic', align_corners=False)
    x = F.interpolate(x[:, :, top:bottom, left:right],
                      size=(H, W), mode='bicubic', align_corners=False)

    return x_rec, x
```

Note that our padding-and-trimming operation includes downsampling with a random ratio. We assume that this random downsampling provides a generative model with diversified signals in backpropagation across training iterations, which makes the model more generalizable.

Figure 11 shows images reconstructed by an RSQ-VAE model trained with a normal LPIPS loss, $\mathcal{L}_{\text{LPIPS}}(\boldsymbol{x}, \boldsymbol{f}_{\boldsymbol{\theta}}(\boldsymbol{Z}_{1:L}))$, and ones reconstructed by an RSQ-VAE model trained with our modified LPIPS loss, $\mathcal{L}_{\text{LPIPS}}(\text{pt}\,[\boldsymbol{x}]\,, \text{pt}\,[\boldsymbol{f}_{\boldsymbol{\theta}}(\boldsymbol{Z}_{1:L})])$. As shown, our padding-and-trimming technique alleviates the artifacts issue. For example, vertical line noise can be seen in hairs in the images generated by the former model, but those lines are removed or softened in the images generated by the latter model. Indeed, our technique improves rFID from 10.07 to 8.47.

C.5 Progressive coding

For demonstration purpose of Figure 4a, we incorporate the concept of *progressive coding* Ho et al. (2020); Shu & Ermon (2022) to our framework, which helps hierarchical models to be more sophisticated in progressive lossy compressing and may generate high-fidelity samples. One can train SQ-VAE-2 to achieve progressive lossy compression (as in Figure 4a) by introducing additional generative processes $\tilde{\boldsymbol{x}}_l \sim \mathcal{N}(\tilde{\boldsymbol{x}}_l; \boldsymbol{f}_{\boldsymbol{\theta}}(\boldsymbol{Z}_{1:l}), \sigma_l^2 \boldsymbol{I})$ for $l \in [L]$. We here derive the corresponding ELBO objective with this concept. Its benefit is to produce more reasonable reconstructed images only with higher layers (i.e., using only low-resolution information $\boldsymbol{H}_{\boldsymbol{\phi}}^r(\boldsymbol{x})$).

First, we consider corrupted data $\tilde{\boldsymbol{x}}_l$ for $l \in [L]$, which is obtained by adding noises, for example, i.e., $\tilde{\boldsymbol{x}}_l = \boldsymbol{x} + \boldsymbol{\epsilon}$. We here adopt the Gaussian distribution $\epsilon_{l.d} \sim \mathcal{N}(0, v_l)$ for the noises. Note that $\{\sigma_l^2\}_{l=1}^L$ is set to be a non-increasing sequence. We model the generative process using only the top l groups as

$p^l_{\boldsymbol{\theta}}(\tilde{\boldsymbol{x}}_l) = \mathcal{N}(\tilde{\boldsymbol{x}}_l; \boldsymbol{f}_{\boldsymbol{\theta}}(\boldsymbol{Z}_{1:l}), \sigma_l^2 \boldsymbol{I})$. Now the ELBO is obtained as

$$\mathcal{J}^{\text{prog}}_{\text{SQ-VAE-2}} = \sum_{l=1}^{L} \frac{D}{2} \log \sigma_l^2 + \mathbb{E}_{\mathcal{Q}(\boldsymbol{Z}_{1:L}, \tilde{\boldsymbol{Z}}_{1:L}|\boldsymbol{x})} \left[\frac{\|\boldsymbol{x} - \boldsymbol{f}_{\boldsymbol{\theta}}(\boldsymbol{Z}_{1:l}) + D v_l\|_2^2}{2\sigma_l^2} + \frac{\|\tilde{\boldsymbol{Z}}_l - \boldsymbol{Z}_l\|_F^2}{2 s_l^2} - H(\hat{P}_{s_l^2}(\boldsymbol{Z}_l|\tilde{\boldsymbol{Z}}_l)) \right] \tag{29}$$

In Section 5.3, we simply set $v_l = 0$ in the above objective when this technique is activated.

This concept can be also applied to the hybrid model derived in Appendix B by considering additional generative processes $p^r_{\boldsymbol{\theta}}(\tilde{\boldsymbol{x}}_r) = \mathcal{N}(\tilde{\boldsymbol{x}}_r; \boldsymbol{f}_{\boldsymbol{\theta}}(\boldsymbol{Z}_{1:L_r}), \sigma_r^2 \boldsymbol{I})$. The ELBO objective is as follows:

$$\begin{aligned}\mathcal{J}^{\text{prog}}_{\text{HQ-VAE}} &= \sum_{r=1}^{R} \frac{D}{2} \log \sigma_r^2 \\ &+ \mathbb{E}_{\mathcal{Q}(\boldsymbol{Z}_{1:L}, \tilde{\boldsymbol{Y}}_{1:R}|\boldsymbol{x})} \left[\sum_{r=1}^{R} \frac{\|\boldsymbol{x} - \boldsymbol{f}_{\boldsymbol{\theta}}(\boldsymbol{Z}_{1:L_r}) + D v_r\|_2^2}{2\sigma_r^2} + \sum_{r=1}^{R} \frac{\left\| \hat{\boldsymbol{Y}}_r - \sum_{l \in \ell_r} \boldsymbol{Z}_l \right\|_F^2}{2 \sum_{l \in \ell_r} s_l^2} - \sum_{l=1}^{L} H(\hat{P}_{s_l^2}(\boldsymbol{Z}_l|\tilde{\boldsymbol{Z}}_l)) \right]. \end{aligned} \tag{30}$$

In Section C.3, we simply set $v_l = 0$ in the above objective when this technique is activated.

D Application of HQ-VAE to image generation

To demonstrate the applicalability of HQ-VAE to generation tasks, we train a prior model on the FFHQ latent features extracted by RSQ-VAE using a contextual RQ-Transformer (Lee et al., 2022b). Figure 13 shows the generated samples from RSQ-VAE with the prior. Accordingly, the latent representations learned by HQ-VAEs are shown to be tractable for prior models.

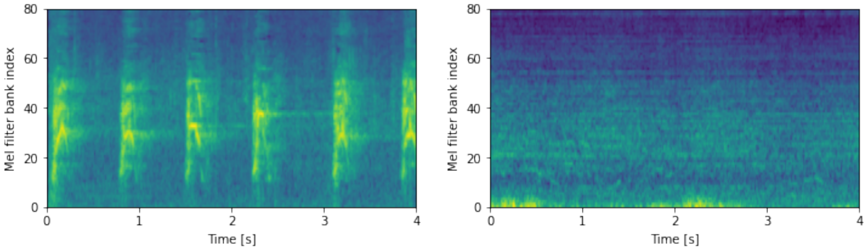

(a) Source.

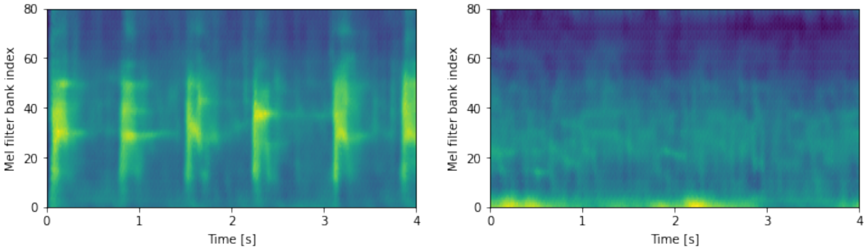

(b) RQ-VAE with 4 layers.

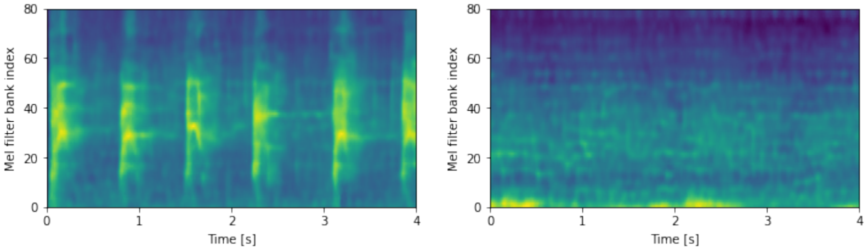

(c) RQ-VAE with 8 layers.

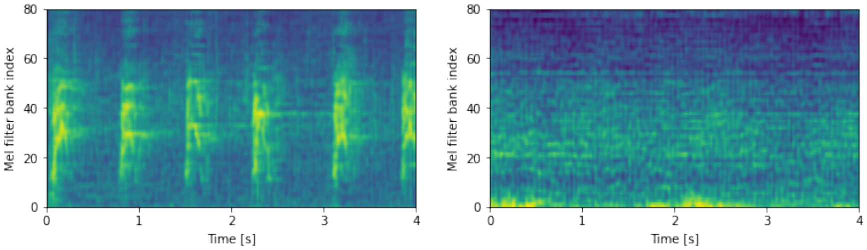

(d) RSQ-VAE with 4 layers.

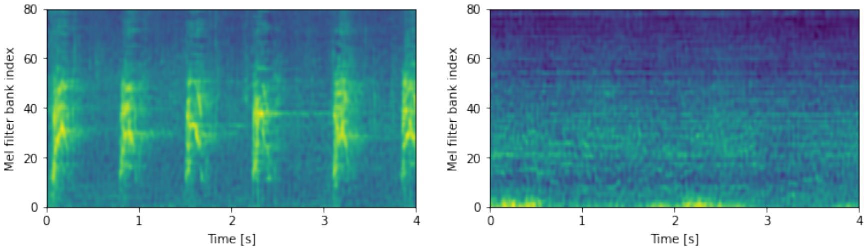

(e) RSQ-VAE with 8 layers.

Figure 10: Mel spectrogram of (a) sources and (b)-(e) reconstructed samples of UrbanSound8K dataset. The left panel and the right panel are audio clips of dog barking and drilling, respectively. We observe that RQ-VAEs struggle to reconstruct the sources with shared codebooks. In contrast, the reconstruction of RSQ-VAE can reflect the details of the source samples.

(a) Source

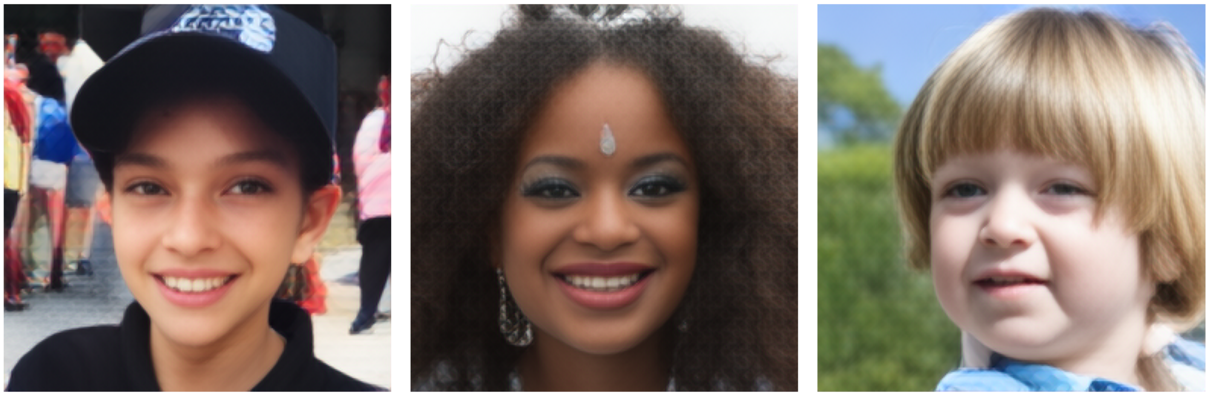

(b) RSQ-VAE trained with a normal LPIPS loss (rFID= 10.07)

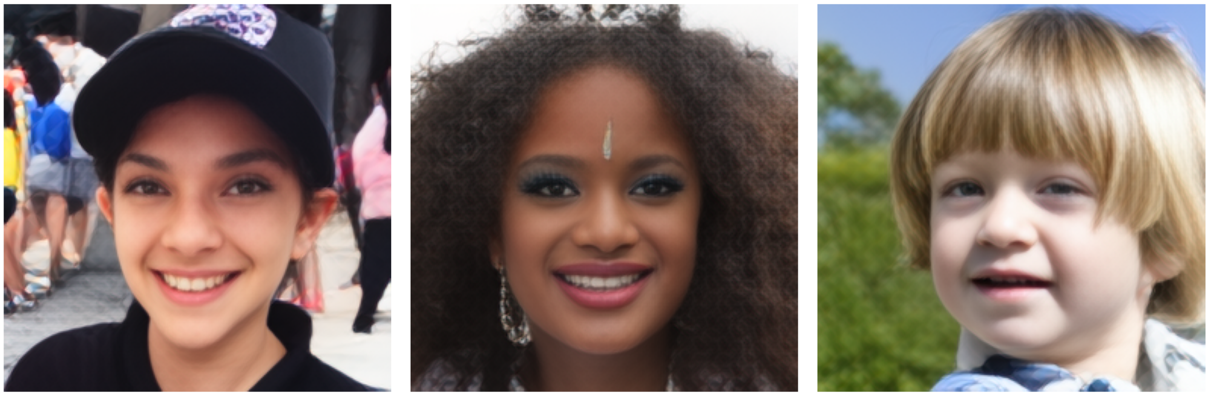

(c) RSQ-VAE trained with our improved LPIPS loss (rFID= 8.47)

Figure 11: Reconstructed samples of FFHQ.

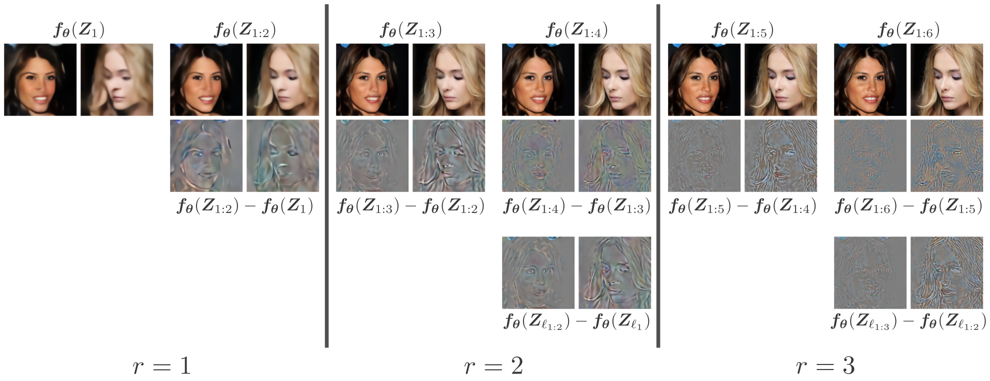
$f_\theta(Z_1)$
$f_\theta(Z_{1:2})$
$f_\theta(Z_{1:3})$
$f_\theta(Z_{1:4})$
$f_\theta(Z_{1:5})$
$f_\theta(Z_{1:6})$
$f_\theta(Z_{1:2}) - f_\theta(Z_1)$
$f_\theta(Z_{1:3}) - f_\theta(Z_{1:2})$
$f_\theta(Z_{1:4}) - f_\theta(Z_{1:3})$
$f_\theta(Z_{1:5}) - f_\theta(Z_{1:4})$
$f_\theta(Z_{1:6}) - f_\theta(Z_{1:5})$
$f_\theta(Z_{\ell_{1:2}}) - f_\theta(Z_{\ell_1})$
$f_\theta(Z_{\ell_{1:3}}) - f_\theta(Z_{\ell_{1:2}})$
$r = 1$
$r = 2$
$r = 3$

(a) Case1: $\ell_1 = \{1, 2\}$, $\ell_2 = \{3, 4\}$ and $\ell_3 = \{5, 6\}$

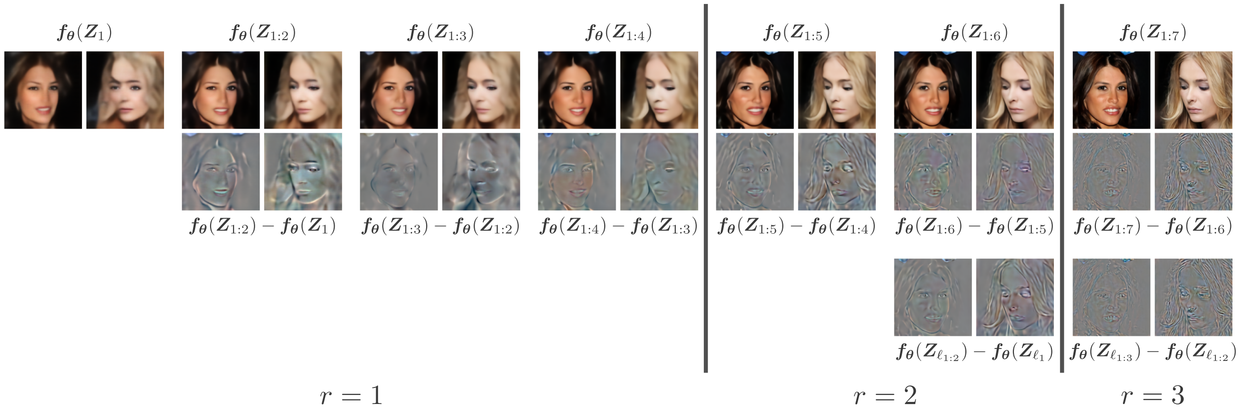
$f_\theta(Z_1)$
$f_\theta(Z_{1:2})$
$f_\theta(Z_{1:3})$
$f_\theta(Z_{1:4})$
$f_\theta(Z_{1:5})$
$f_\theta(Z_{1:6})$
$f_\theta(Z_{1:7})$
$f_\theta(Z_{1:2}) - f_\theta(Z_1)$
$f_\theta(Z_{1:3}) - f_\theta(Z_{1:2})$
$f_\theta(Z_{1:4}) - f_\theta(Z_{1:3})$
$f_\theta(Z_{1:5}) - f_\theta(Z_{1:4})$
$f_\theta(Z_{1:6}) - f_\theta(Z_{1:5})$
$f_\theta(Z_{1:7}) - f_\theta(Z_{1:6})$
$f_\theta(Z_{\ell_{1:2}}) - f_\theta(Z_{\ell_1})$
$f_\theta(Z_{\ell_{1:3}}) - f_\theta(Z_{\ell_{1:2}})$
$r = 1$
$r = 2$
$r = 3$

(b) Case2: $\ell_1 = \{1, 2, 3, 4\}$, $\ell_2 = \{5, 6\}$ and $\ell_3 = \{7\}$

Figure 12: Reconstructed images and magnified differences of HQ-VAE on CelebA-HQ

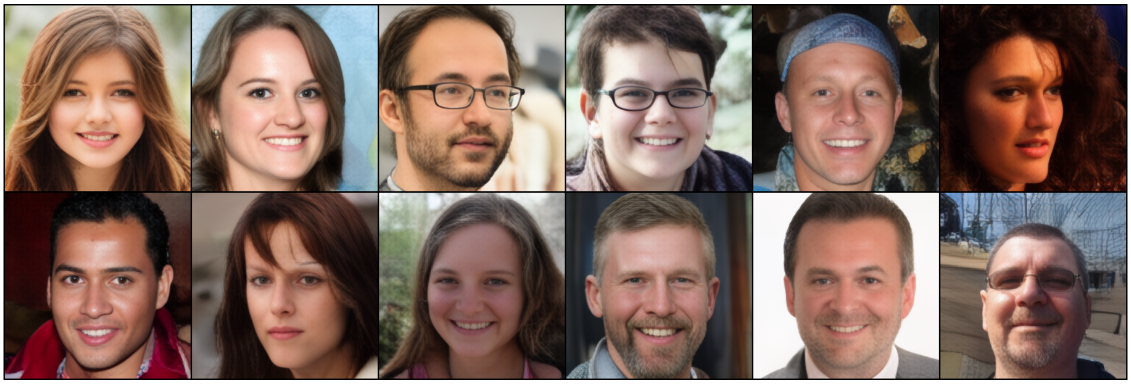

Figure 13: Samples of FFHQ from RSQ-VAE with contextual RQ-Transformer (Lee et al., 2022b).